Geochemistry xxx (xxxx) xxx

Contents lists available at ScienceDirect

Geochemistry

journal homepage: www.elsevier.com/locate/chemer

The magmatic to post-magmatic evolution of the Nooitgedacht Carbonatite Complex, South Africa☆

Mohsin Raza [a,b,c,*], R. Johannes Giebel [d,e], Sebastian Staude [f], Aratz Beranoaguirre [a,b], Jochen Kolb [a,b], Gregor Markl [f], Benjamin F. Walter [a,b,f]

[a] Karlsruhe Institute of Technology (KIT), Chair of Economic Geology and Geochemistry (EGG), Adenauerring 20b, 76131 Karlsruhe, Germany
[b] Karlsruhe Institute of Technology (KIT), Laboratory for Environmental and Raw Material Analyses (LERA), Adenauerring 20b, 76131 Karlsruhe, Germany
[c] Department of Geology, Bacha Khan University Charsadda, Pakistan
[d] Technische Universität Berlin, Applied Geochemistry, Ernst-Reuter-Platz 1, 10587 Berlin, Germany
[e] University of the Free State, Department of Geology, 250 Nelson-Mandela-Drive, Bloemfontein 9300, South Africa
[f] University of Tübingen, Petrology and Mineral Resources, Schnarrenbergstrasse 94-96, 72076 Tübingen, Germany

ARTICLE INFO

Handling Editor: Vincenza Guarino

Keywords:
Apatite mineral chemistry
Pyrochlore compositional variations
REE mineralization
Critical metals
Crustal contamination

ABSTRACT

Carbonatites are unusual, mantle-derived igneous rocks characterized by distinctive mineralogical and geochemical fingerprints that may decipher complex processes during their multi-stage evolution. A systematic petrographic, whole rock geochemistry, apatite and pyrochlore mineral chemistry, U-Pb geochronology, and C-O stable isotope study was performed on the carbonatites of the Nooitgedacht Carbonatite Complex in the Republic of South Africa in order to understand their genesis and evolution including the significant differences in the nature of their HFSE-REE endowment. Early carbonatite intrusion is reflected by a plug-like calcite carbonatite. A second stage carbonatite intrusion formed a ring-shaped, quartz-Fe-dolomite-calcite carbonatite comprising apatite and monazite. The third stage of carbonatite intrusion formed dolomite carbonatite dikes. The calcite carbonatite exhibits a well-developed magmatic stage characterized by the presence of oscillatory zoned, F-rich pyrochlore, pill-shaped apatite, magnetite and forsterite, while the hydrothermal stage is indicated by the presence of quartz, baryte, massive apatite, bastnäsite, and monazite. Although the second carbonatite generation is very similar to the first generation in terms of mineralogy, the hydrothermal overprint in particular is much more pronounced in the later. The third carbonatite generation, however, differs significantly from its two predecessors mineralogically and does not show any hydrothermal overprint. Whole rock ΣREE concentrations in early stage carbonatite range between 380 and 2200 ppm, the quartz-Fe-dolomite-calcite carbonatite shows a higher ΣREE concentrations between 3010 and 5900 ppm, while the third stage dolomite carbonatite has ΣREE concentrations between 574 and 2239 ppm. This trend follows a positive correlation with the degree of alteration, as REE mineralization occurs mainly in the hydrothermal post-magmatic stage. Pyrochlore observed in early calcite carbonatite shows oscillatory zoning overgrowing U-Ta rich resorbed cores (entrained from associated syenite). Pyrochlores observed in quartz-Fe-dolomite-calcite carbonatites exhibit relicts of fluorcalciopyrochlore (magmatic stage) overgrown by hydroxycalciopyrochlore (hydrothermal stage: characterized by patchy zonation) and hydropyrochlore (supergene stage: mainly characterized by narrow rims around the pyrochlore grains). Textural and compositional variations in apatite further allow tracking the evolution of Nooitgedacht carbonatites. Pill and ovoidal shaped apatites from calcite carbonatite and quartz-Fe-dolomite-calcite carbonatite, respectively, with marginal higher Si and less F concentrations shows a magmatic origin, while irregular apatite masses from calcite carbonatite and quartz-Fe-dolomite-calcite carbonatite (with higher Sr and F concentrations) suggest a hydrothermal origin. However, the dolomite carbonatite (third intrusion stage) lack both, apatite and pyrochlore. The in-situ U-Pb geochronology in calcite carbonatite (apatite and pyrochlore ~1330 Ma) and quartz-Fe-dolomite-calcite carbonatite (apatite ~1280 Ma) suggested two different magmatic events. The two different ages of carbonatite intrusion, furthermore, suggest the reuse of the same path way system during the carbonatite melt ascent. Stable isotope compositions for early stage carbonatite plot

☆ This article is part of a special issue entitled: News in carbonatite world published in Geochemistry.

* Corresponding author at: Karlsruhe Institute of Technology (KIT), Chair of Economic Geology and Geochemistry (EGG), Adenauerring 20b, 76131 Karlsruhe, Germany.
E-mail address: mohsin.raza@kit.edu (M. Raza).

https://doi.org/10.1016/j.chemer.2025.126249
Received 18 July 2024; Received in revised form 30 November 2024; Accepted 13 January 2025
Available online 16 January 2025

within the primary igneous carbonatite field, while the compositions for quartz-Fe-dolomite-calcite carbonatite and dolomite carbonatite follows a trend from lower to higher values either due to contamination/wall rock interaction during ascent or due to Rayleigh fractionation. Based on the above data, we proposed a magmatic to post-magmatic (hydrothermal/supergene) evolution (including a ~50 Ma gap between the early and the later carbonatite) with enrichment of REE in the later stage carbonatite due to hydrothermal activity.

1. Introduction

Carbonatites are defined as igneous rocks predominantly constituted of carbonate minerals (>50 modal%), with accessories of phosphates, silicates, and oxides (Yaxley et al., 2022). Their predominant carbonate phases classify carbonatites into calcite, dolomite, nyerereite/gregoryite (only predominantly present at Oldoinyo Lengai and Kerimasi), or ankerite/siderite carbonatites (Gittins and Harmer, 1997; Le Maitre, 2002). 454 carbonatite occurrences (intrusive and extrusive; Schmidt et al., 2024), which appear in a variety of shapes and sizes, such as dykes, plugs, cone sheets, sills, volcanic necks, etc., are located across the globe (Yaxley et al., 2022). Calcite carbonatites are the most prevalent carbonatites. Dolomite- and ankerite/siderite carbonatites are rather subordinate and often form inner cores, dykes or other late intrusions crosscutting the main calcite carbonatite bodies (Gudelius et al., 2023; Kamenetsky et al., 2021; Walter et al., 2021; Yaxley et al., 2022). 80 % of these occurrences are associated with alkali-rich silicate intrusions (Humphreys-Williams and Zahirovic, 2021; Mitchell, 2005).

The origin of carbonatite melts is explained by (1) direct formation via low-degree partial mantle melting (Bell and Simonetti, 2010) or (2) a derivation from a carbonate-bearing silicate melt via fractional crystallization and/or liquid-liquid immiscibility (Jones et al., 2013; Lee and Wyllie, 1997; Mitchell, 2005; Yaxley et al., 2022). Their ascent follows transcrustal zones of weak whereby the intrusion of carbonatites is often linked to continental rift settings or suture zones (Woolley and Kjarsgaard, 2008). During their ascent into shallow crustal levels carbonatites might experience several evolutionary (magmatic and post-magmatic) events, including (i) a probable separation of different immiscible melts (i.e., fluoride, sulfide, and oxide melts), (ii) crystal fractionation, (iii) magma – wall-rock interaction/contamination, (iv) metasomatic 'antiskarn' formation, (v) the evolution into a 'brine-melt' (carbothermal fluid) and (vi) the exsolution of aqueous-carbonic (hydrothermal) fluids of varying salinity (Demény et al., 1998; Jones et al., 2013; Giebel et al., 2019a,b; Anenburg et al., 2021; Walter et al., 2021; Stoppa, 2021).

Carbonatites are known as important deposits of critical raw materials and represent significant exploration targets for Rare Earth Elements (REEs) due to their high concentration of Light Rare Earth Elements (LREEs), size, and often extraction-friendly mineralogy (Chakhmouradian and Wall, 2012; Goodenough et al., 2016; Verplanck et al., 2016; Stoppa et al., 2019). However, the nature and degree of REE mineralization of carbonatites differ considerably based on the evolutionary processes they underwent (Broom-Fendley et al., 2017b). Late-magmatic processes are attributed to higher REE enrichment in most explored deposits (Migdisov et al., 2014; Wan et al., 2021; Williams-Jones and Artas, 2014). Thus, higher-evolved dolomite- and ankerite/siderite-carbonatites are anticipated to depict higher REE contents. Recent studies have revealed that in both early and late magmatic stages, carbonatite–wall rock interaction may significantly influence REE enrichment (Anenburg and Mavrogenes, 2018; Walter et al., 2021; Yaxley et al., 2022).

To reveal the nature and influence of the different evolutionary stages of a carbonatite, it is crucial to study carbonatite complexes comprising individual carbonatites characterized by varying degrees of effects of the different stages. Ideally, these carbonatites share very similar mineralogical preconditions. Such an investigation can also provide important information about the behavior of REE mineralization within such a multi-stage system. According to these requisites, the Nooitgedacht complex in the Republic of South Africa is an ideal natural laboratory to test indicators/proxies that identify a specific evolutionary stage, to investigate the mineralogical and mineral chemical influence of corresponding stages and to specify the corresponding effect on REE mineralization in carbonatites, as REE-poor calcite carbonatites (dominated by magmatic mineralization) and REE-rich quartz-Fe-dolomite-calcite carbonatites (dominated by post-magmatic hydrothermal mineralization) occur together. This research, moreover, provides the first comprehensive description of the Nooitgedacht carbonatite.

2. Geological setting

The Nooitgedacht carbonatite is situated within the central northern part of the Archean Kaapvaal Craton (KC, Fig. 1A), which is divided into four major tectonostratigraphic terrains, namely the Kimberley (~3.0–2.8 Ga), Pietersburg (~3.0–2.8 Ga), Witwatersrand (~3.3–2.8 Ga), and Swaziland (3.6–3.1 Ga) blocks. These terrains are separated by deep-reaching structural/tectonic features known as the Thabazimbi-Murchison Lineament (TML), the Colesburg Lineament (CL), and the Barberton Lineament (BL; Friese et al., 2003). The northern KC border is mainly characterized by the Palala-Zoetfontein (PSZ) and Hout river Shear Zones (HRSZ).

The northern part of the KC exhibits the Bushveld Igneous Complex (BIC). BIC is an ultramafic layered intrusion that intruded the Transvaal Supergroup at ~2.055 Ga (Hatton and Schweitzer, 1995; Scoates and Friedman, 2008; Walraven et al., 1992; Yudovskaya et al., 2023). A further prominent intrusion represents the alkaline Pilanesberg complex (as the main intrusion of the Pilanesberg Alkaline Province; Verwoerd, 2006) that emplaced into the western BIC at ~1.395 Ga (Elburg and Cawthorn, 2017).

Within the Kaapvaal craton, carbonatites were emplaced at two distinct times during the Proterozoic, which show either a temporal affinity to the Bushveld or the Pilanesberg events. The oldest carbonatites include the Palabora and Schiel complexes (emplaced at ~2.06 Ga). According to their temporal and spatial (north-eastwards of the BIC) relation to the Bushveld Igneous Complex (~2.055 Ga), these carbonatites are grouped as "Bushveld carbonatites". Younger carbonatites intruded the Transvaal Supergroup and BIC between ~1.45 and ~1.20 Ga (Harmer, 1999). According to their temporal and partly spatial proximity to the Pilanesberg intrusion, these carbonatites are assigned to the Pilanesberg Alkaline Province and grouped as "Pilanesberg carbonatites" (Ferguson, 1973). This includes the following alkaline and carbonatite complexes, and grouped subprovinces: The Spitskop Complex (and Magnet Hights), Goudini Complex, Glenover Complex, Stukpan Complex, Pienaars River Subprovince, and Crocodile River Subprovince (Verwoerd, 1967).

The Pienaars River Subprovince (also known as the Franspoort Line) includes the Derdeport Carbonatite Complex and several alkaline complexes (Ferguson, 1973; Verwoerd, 1967). The Crocodile River Subprovince includes the Nooitgedacht Carbonatite Complex, the carbonatitic Kruidfontein Volcanic Complex, Tweerivier Carbonatite Complex, Bulhoek (Bulhoekkop and Bulhoek South) carbonatites, Welgevonden (West and East) carbonatites and the Buffelskraal Alkaline Complex (not exposed; no carbonatites; Verwoerd, 1993).

The Crocodile River Subprovince is situated on the Crocodile River Fragment (western BIC), an inlier of intensely deformed rocks of the Transvaal Sequence, which is mainly enclosed by Bushveld granite of the Lebowa granite suit (mainly Nebo granite; Eriksson and Reczko,

1995). Within this subprovince the Buffelskraal, Nooitgedacht and Tweerivier complexes, as well as Welgevonden East, clearly follow a north-south emplacement trend, while Bulhoekkop, Bulhoek South, and Welgevonden West show a slightly diverge (clockwise rotated) alignment from this trend (NNE-SSW, Fig. 1B). The Kruidfontein Volcanic Complex represents the pivotal centre of both orientation trends.

2.1. The Nooitgedacht Carbonatite Complex

The Nooitgedacht Carbonatite Complex is a plug-like, slightly irregular oval body (about 2 km long and 3 km wide, Fig. 1C), which intruded quartzites and black shales of the Black Reef formation, and limestones and dolomites of the Wachteenbeetje formation (exclusively situated at the northern boundary of the complex). The complex is unaffected by any folding, faulting and metamorphism (Verwoerd, 1967). However, due to extensive weathering, the complex is poorly exposed.

Besides carbonatites, which represent the most abundant lithologies, the complex also contains syenite, nepheline syenite, phonolite, and a 500 m wide zone of fenite (indicated by isolated outcrops). Among the carbonatites, three different types can be identified, namely calcite carbonatite, quartz-Fe-dolomite-calcite carbonatite (previously named as quartz-parankerite søvite) and dolomite-carbonatite (Schürmann et al., 1997; Verwoerd, 1967). Calcite carbonatite is the main carbonatite type, occurs as a plug-like body and represents the first generation of carbonatite intrusion (Fig. 2A, B). Quartz-Fe-dolomite-calcite carbonatite forms ring dykes (present near the centre of the calcite carbonatite intrusion) as a second generation of carbonatite intrusion (Fig. 2C–F). Dolomite carbonatite occurs as 1–2 m wide and up to 450 m long dykes (central stockwork) and represents the youngest carbonatite intrusion of the complex (Verwoerd, 1967). The dolomite carbonatite is in conformable contact with the flow structure of calcite carbonatites (Fig. 2A), but also occasionally intersects it.

3. Analytical methods

3.1. Sample material and data

A detailed fieldwork was carried out in 2021, during which forty-six samples were collected from outcrops of the Nooitgedacht complex. After careful macroscopic examination, forty-two representative samples from various carbonatites were cut into thin sections for petrography, mineral chemistry, and geochronology.

3.2. Electron-microscopy (petrography)

A TESCAN VEGA II, coupled with an EDX INCAx-act scanning electron microscope (SEM) from Oxford Instruments, was used to examine microtextures using backscattered electron (BSE) imaging at the Chair of

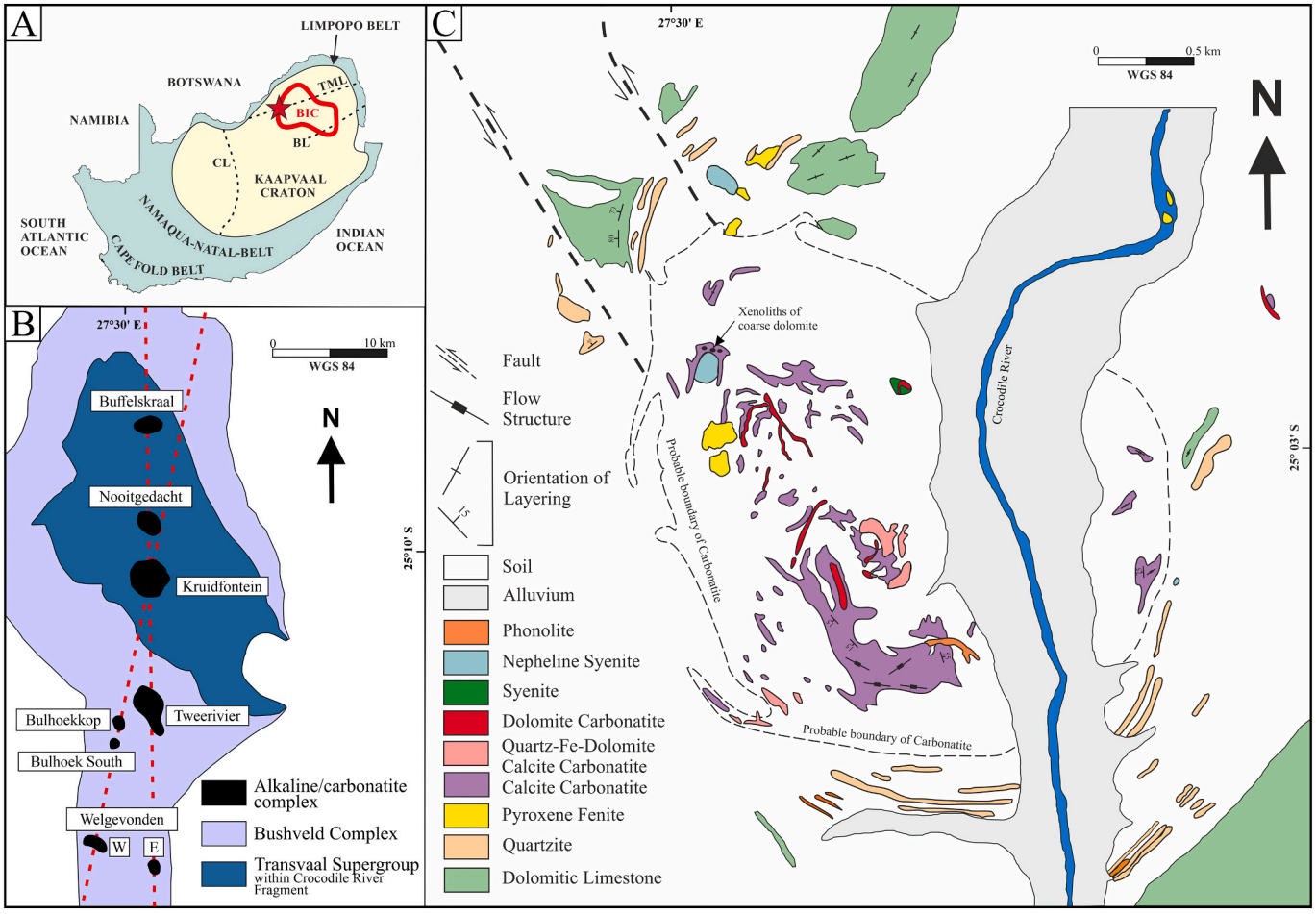

Fig. 1. Geological overview of the Nooitgedacht Carbonatite and its location. (A) Location of Nooitgedacht (Red Star) within the northern Kaapvaal Craton (South Africa); BIC = Bushveld Igneous Complex (mafic phase), BL = Barberton Lineament, CL = Colesberg Lineament, and TML = Thabazimbi-Murchison Lineament (map modified after Friese et al., 2003). (B) Geometric relationship between Nooitgedacht and the spatially associated complexes of Buffelskraal, Tweerivier, Welgevonden East (E in figure) (all N-S aligned), Bulhoekkop, Bullhoek South, Welgevonden West (W in figure) (NNE-SSW aligned) and Kruidfontein (central position). (C) Geological map of the Nooitgedacht complex (modified after Verwoerd, 1967). (For interpretation of the references to colour in this figure legend, the reader is referred to the web version of this article.)

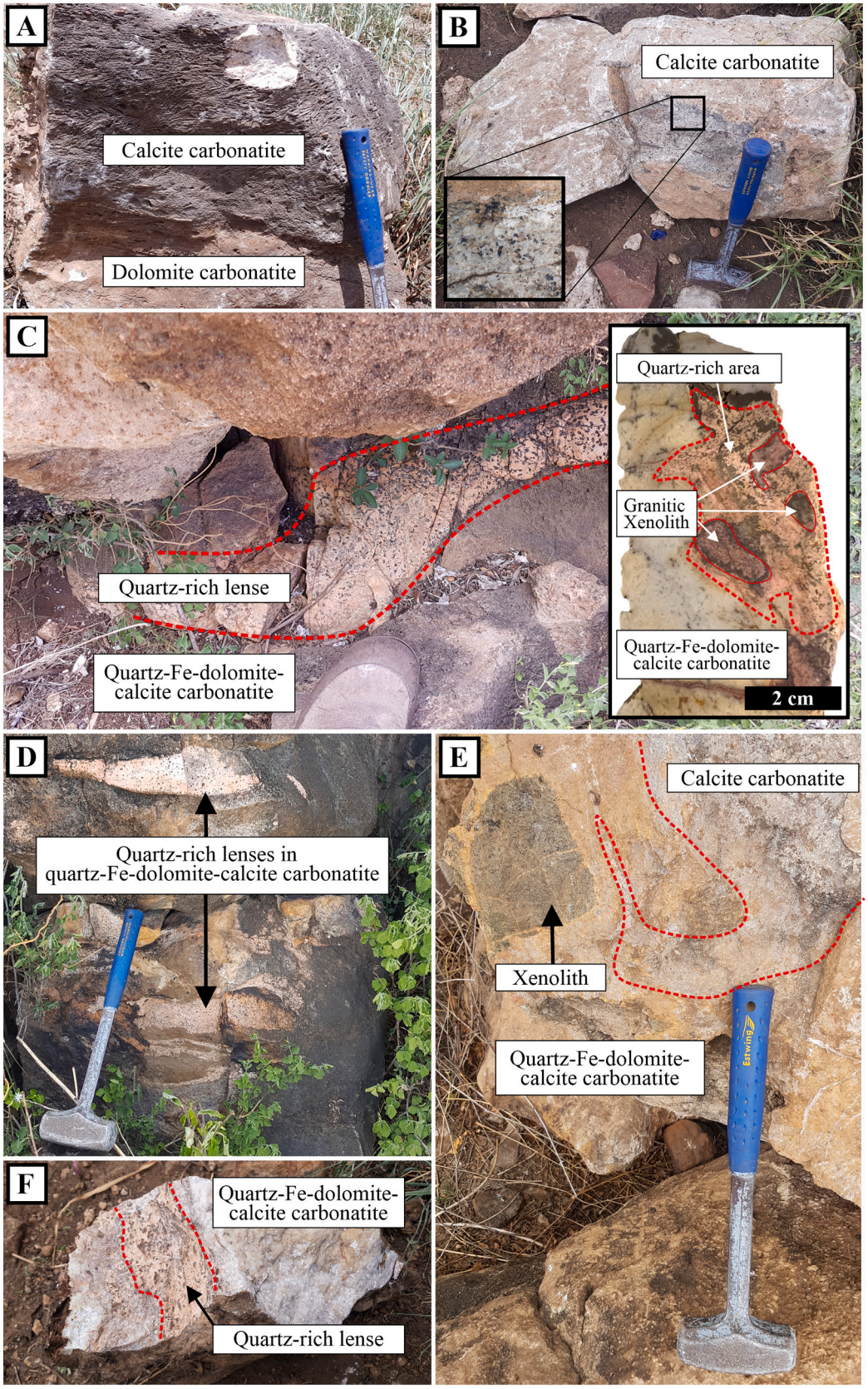

Fig. 2. Field Images. (A) Contact between calcite carbonatite and dolomite carbonatite. (B) Calcite carbonatite with magnetite and pyrochlore grains. (C) Late stage quartz-Fe-dolomite-calcite carbonatite including a quartz-rich lens (shoe tip for scale). Small inlier shows quartz-rich lens that forms at the expense of Nebo granite xenoliths (visible as relicts). (D) Localized quartz enrichment in quartz-Fe-dolomite-calcite carbonatites. (E) Contact between calcite carbonatite and quartz-Fe-dolomite-calcite carbonatite; with the latter including a xenolith. (F) Hand specimen showing the (fresh) contact between quartz-Fe-dolomite-calcite carbonatite and a quartz-rich lens.

Mineralogy and Petrology, Karlsruhe Institute of Technology, Germany. Experimental settings for the SEM were 10 nA beam current and 15 kV acceleration voltage.

3.3. XRF and ICP-MS (whole-rock geochemistry)

For whole-rock major elements (CaO, MgO, MnO, Fe_2O_3, Na_2O, K_2O, SiO_2, Al_2O_3, P_2O_5, and TiO_2) the Laboratory for Environmental and Raw Material Analysis (LERA) at Karlsruhe Institute of Technology (KIT) utilized wavelength dispersive X-ray fluorescence (WD-XRF, S4 Explorer, Bruker AXS) apparatus. Fused beads were examined with 10:1 Lithium tetraborate: sample ratio. The sample was heated up to 950 °C for 3 h for loss on ignition (LOI) determination. Certified reference materials (JDO-1, SY-2, PCC-1, SARM 5, RGM-1, and AGV-1) were used to guarantee 1–6 % analytical accuracy.

Thermo Fisher Scientific's iCAP RQ instrument measured bulk samples' trace element and REE concentration using ICP-MS after acid digestion of 100 mg powder. To completely dissolve the silicate minerals, the sample was heated with 40 % HF (supra pure), 65 % $HClO_4$ (normatom), and pre-oxidized (65 % HNO_3, sub-boiled) acid in a covered Teflon tank at 120 °C for 16 h. The residue was cleansed and redissolved in either 65 % HNO_3 (subboiled, silicates) or 30 % HCl (normatom, carbonatite) after the acids were evaporated in open containers. The ultimate residue was absorbed by 2 ml of 65 % HNO_3 (subboiled) and subsequently diluted in 50 ml of ultrapure water. The precision of the ICPMS measurement was in the range of 1 %. Measurements are checked by regularly 100 µg/l standard solutions. Accuracy and precision were checked by certified reference materials (CRM-Sy2 and GRE-03 from High-Purity Standards, Inc.) after every ten samples.

3.4. EMPA (mineral chemistry)

The chemical compositions of apatite and pyrochlore were measured using a Jeol JXA-8230 electron microprobe at the Department of Geoscience, Tübingen, Germany. The electron microprobe was used to analyze apatite using a 15-kV accelerating voltage, 10 nA beam current, and 10 µm defocused beam diameter (to minimize halogen diffusion induced by the electron beam). The ZAF matrix correction method from Armstrong (1991) and Bence and Albee (1968) was used for quantification. A focused beam with 20 kV acceleration voltage and 20 nA beam current was utilized for pyrochlore analyses. Additional WDS setup information is provided in the supplemental electronic documents (ES1).

3.5. Raman spectroscopy

Raman spectroscopy of apatite was performed on polished thin sections. Data were analysed using a Bruker Senterra spectrometer coupled to an Olympus BX51 light microscope at the Institute of Applied Geosciences, Karlsruhe Institute of Technology. A 532 nm laser with a laser power of 5 mW was focused onto apatite with a 50× microscope lens using an aperture of 25 µm and resulting in a spot diameter of c. 2 µm in the focus. Raman spectra were acquired for 50 s with a spectral resolution of 1.3 cm^{-1} and room conditions of 19 °C and 1 bar. Multiple measurements were performed on each apatite. The Bruker Senterra performs an internal calibration on a neon line before every inclusion measurement. The instrument drift was monitored by periodic measurement of a gem-quality quartz polished mount.

3.6. LA-ICP-MS (U-Pb geochronology)

Uranium-Pb age data were collected at the LERA facilities, using a modified method after (Gerdes and Zeh, 2006, 2009). ThermoFisher Element 2 sector field ICP-MS was coupled to a 193-nm ArF Excimer laser with a HelEx 2-volume cell (Beranoaguirre et al., 2022). After two helium ablations, the minerals were combined with argon and nitrogen before the plasma torch. Before each session, the ICP-MS was adjusted for maximum sensitivity and low oxide production (UO/U < 0.2 %) using SRMNIST612 synthetic glass (Jochum et al., 2011). Supplemental Table S1 shows analytical characteristics including gas flow and spot size.

Data was processed using an in-house VBA Microsoft Excel© spreadsheet application (Gerdes and Zeh, 2006, 2009) utilizing Isoplot methods (Ludwig, 2003). For apatite analyses, SRMNIST612 (Jochum et al., 2011) was used to correct mass biases and drift in the $^{207}Pb/^{206}Pb$ and $^{206}Pb/^{238}U$ ratios. Durango (McDowell et al., 2005), Sume (Lana et al., 2022), and in-house apatites (reproducible at 200 Ma) were used to adjust the $^{206}Pb/^{238}U$ ratios for matrix differences. Itambe monazite was used as an additional matrix correction for $^{206}Pb/^{238}U$ ratios for the pyrochlore session (Gonçalves et al., 2016). LA-ICP-MS with non-matrix matched standardisation can accurately date oxide and phosphate minerals (Millonig et al., 2012). All uncertainties were estimated at the 2σ level using recommendations of Horstwood et al. (2016).

3.7. IRMS (stable C-O isotope analysis)

Carbon ($\delta^{13}C$) and oxygen ($\delta^{18}O$) isotope analysis were performed at the LERA, utilizing a Delta V Isotope Ratio Mass Spectrometer and Gas Bench II equipment (Thermo IRMS Delta V Gasbench). At 72 °C, 300 µg of material was acid-reacted in a sealed container for >90 min (reference materials) and >2:5 h (carbonatite samples). Long reaction times and a very fine powder fraction were chosen to allow for complete acid reaction of the different minerals. 100 % phosphoric acid was injected into each vial after it had been flushed with helium. The CO_2 that formed during the reaction of the carbonatite with the acid was flushed with helium through a purification system towards the mass spectrometer (Delta V). Sample measurements were bracketed with working standards, 3 working standard measurements after 10 sample measurements. At the beginning and end of a run, calibration standards were measured. Quality control used Li_2CO_3 and calibration with NBS 18 and an in-house Carrara marble standard. Dolomitic carbonatites were evaluated identical to the calcite carbonatites without correction for the acid fractionation of the dolomitic component. Potential deviations of the dolomitic carbonatite from the true value are on the order of 1 ‰ or lower, due to fraction of dolomitic carbonatite present and the small and diminishing difference between the acid fractionation factor for dolomite and calcite at increasing reaction temperature (Friedman and O'Neil, 1977; Sharma and Sharma, 1969).

4. Results

4.1. Petrography

Based on their mineralogical features (Figs. 3, 4), the carbonatite generations can be distinguished as follows (listed in chronological order of formation):

Type 1 - *Calcite carbonatite*. Carbonatite type 1 represents a generally white fine- to medium-grained (0.5 mm grain diameter) carbonatite (dominated by calcite) with a light grey weathering surface (Fig. 2A). The initial crystallization (ortho-magmatic stage) is reflected by olivine (forsterite) formation (Fig. 3A). Olivine later experienced marginal serpentinization. An early niobium mineralization is characterized by pyrochlore (Fig. 4B). Pyrochlore is irregularly distributed in the calcite carbonatite (Fig. 4A, B), with a modal abundance of 3–5 %. Grains range in colour from pale yellow to dark brown and commonly exhibit an octahedral crystal habit with a grain size of 0.1–1.0 mm. In general, two main textural types of pyrochlore can be distinguished: (a) resorbed bright pyrochlore cores (type i) and (b) oscillatory zoned (primary zoning) pyrochlores (type ii; Fig. 6A–B). Typically, oscillatory zoned pyrochlore overgrowth the resorbed cores. Moreover, they occasionally contain small inclusions of apatite and calcite. Fractures in pyrochlore are generally filled by calcite and apatite (Fig. 3B). *Please note: in a single pyrochlore grain (Fig. 6A), two additional pyrochlore types (type III and IV;*

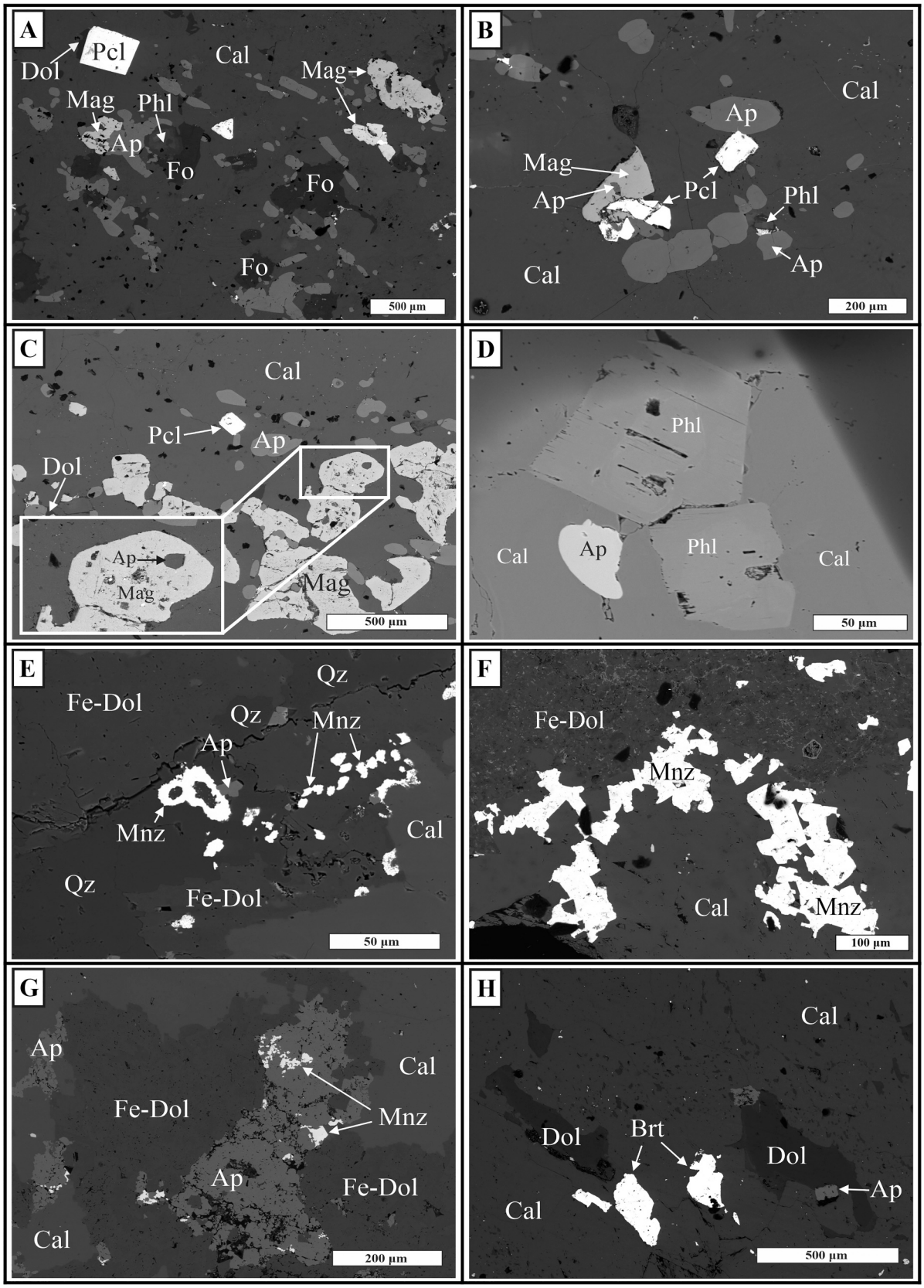

Fig. 3. BSE images showing textural and mineral interrelations in carbonatites. (A, B) Pyrochlore, forsterite, pill shaped apatite, magnetite, and phlogopite association in calcite carbonatite. (C) Magnetite (in calcite carbonatite) with apatite inclusions. (D) phlogopite in calcite carbonatite. (E, F, G) Quartz – apatite – monazite – Fe-dolomite association in quartz-Fe-dolomite-calcite carbonatite. (H) Baryte grains shows hydrothermal imprint in quartz-Fe-dolomite-calcite carbonatite.

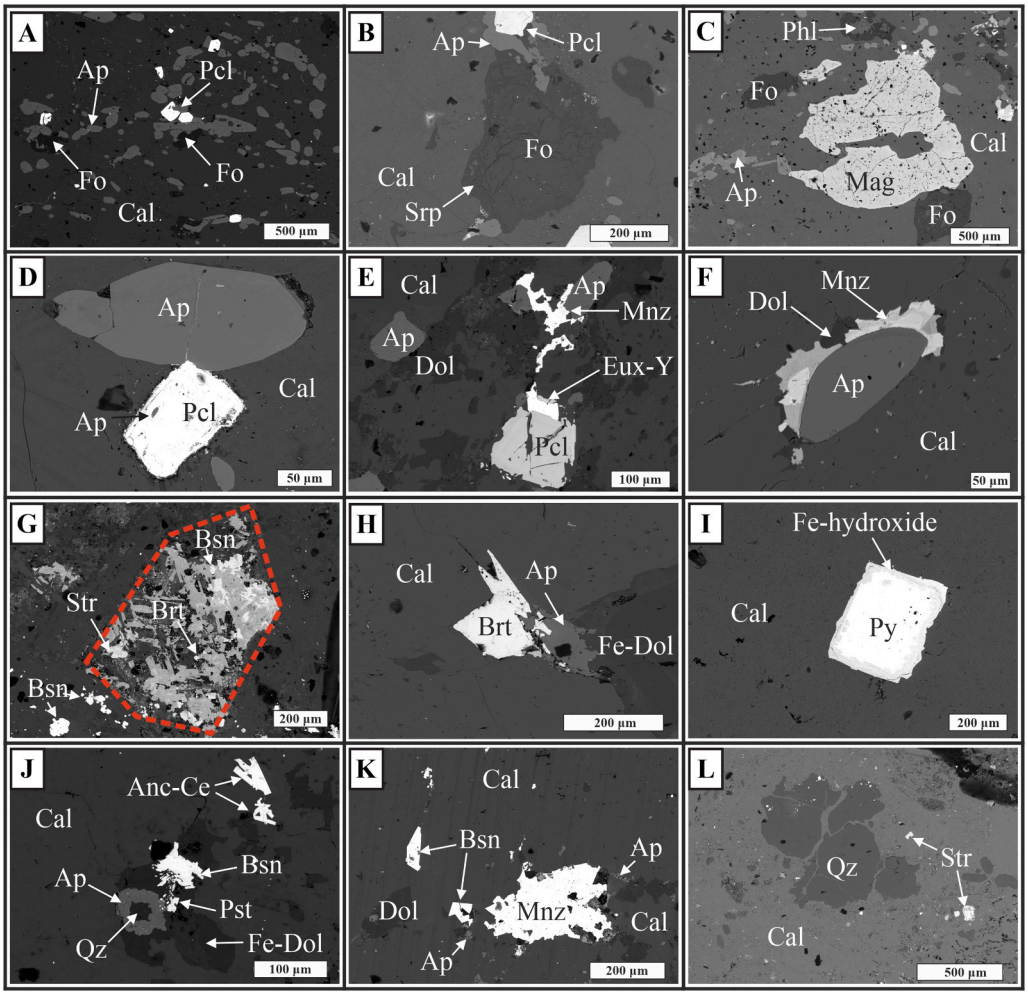

Fig. 4. BSE images showing textural and mineral interrelations in carbonatites. (A) Early crystallized mineral assemblages preserving the igneous textures in calcite carbonatite. (B) Forsterite with serpentinized rims in calcite carbonatite. (C) Magnetite grain with calcite and apatite inclusions (calcite carbonatite). (D) Early pill shaped apatite associated with pyrochlore. (E) Alteration of pyrochlore to euxenite (calcite carbonatite). (F) Monazite formation at the margins of apatite (calcite carbonatite). (G) Pseudomorph of bastnäsite, strontianite and baryte potentially after burbankite. (H) Baryte associated with apatite (type II) and Fe-dolomite in quartz-Fe-dolomite-calcite carbonatite. (I) pyrite altered to Fe-hydroxide (quartz-Fe-dolomite-calcite carbonatite). (J) REE carbonates associated with quartz, apatite and Fe-dolomite in quartz-Fe-dolomite-calcite carbonatite. (K) Monazite and bastnäsite formation in the presence of apatite. (L) Fragment of quartz (xenocryst) in Sr-rich calcite (quartz-Fe-dolomite-calcite carbonatite).

see below) are identified, combining the typical features of carbonatite type 1 and 2; however, this multi-zonal appearance of pyrochlore is not typical for carbonatite type 1.

Apatite show two different varieties, which form early (ortho-magmatic) pill shaped (prismatic) crystals up to 1 cm (often clustered as aggregates, Type-I; Fig. 7A), and late (late-magmatic stage) massive masses (Type-II). This pill shaped apatite shows simple core-rim zonation. The massive apatite is spongey, which likely indicates partial apatite dissolution (Fig. 7B). Magnetite (paragenetically associated with pill shaped apatite and phlogopite) is found as octahedral and irregular anhedral crystals, which often define flow banding orientations in calcite carbonatite (Fig. 4A–D). Calcite and apatite inclusions can be observed in magnetite (Fig. 3C). Euhedral to subhedral phlogopite shows zoning with a dark rim (low average atomic number, AZ) and brighter core (high AZ; Fig. 3D). Carbonate formation spans most of the formation sequence covering the ortho-magmatic, late magmatic and post-magmatic stages. Early carbonate formation is reflected by high-Sr calcite crystallization. A contemporaneous dolomite formation (only as a minor phase) starts at the intermediate stage of high-Sr calcite formation. During the transition from the ortho-magmatic to late magmatic stadium high-Sr calcite formation is followed by low-Sr calcite precipitation. Accessory minerals such as pyrite, monazite (formation around apatite, Fig. 4F), and bastnäsite form as well.

A post-magmatic overprint of the carbonatite is finally clearly highlighted by the subsequent formation of baryte, celestite and strontianite in vugs (probably alteration of burbankite, Fig. 4G), which is often accompanied by the precipitation of further REE carbonates (bastnäsite, parisite and ancylite) together with quartz (Fig. 4J, K). Additionally, this overprint is characterized by the alteration of pyrochlore to euxenite (Fig. 4E) and the oxidation of pyrite and magnetite (formation of Fe-oxide/hydroxide) (Fig. 4I).

Type 2 - *Quartz-Fe-dolomite-calcite carbonatite*. Carbonatite type 2 characterizes a white fine- to medium-grained (0.5 mm grain diameter) calcitic carbonatite with patches of Fe-rich dolomite and a slightly brownish weathering surface. The quartz-Fe-dolomite-calcite carbonatite generally shares the mineralogical characteristics of calcite carbonatites at Nooitgedacht, but differs mostly in the modal abundance of certain minerals. However, some modifications/additions are present. For example, quartz-Fe-dolomite-calcite carbonatite does not contain any olivine and the presence of magnetite is much less common. Quartz may occur as clustered fragments (xenocrysts) (Fig. 4L) or as anhedral masses. Dolomite appears in irregular shapes (0.1–0.2 mm in diameter)

included in calcite and is typically associated with apatite. Dolomite is much more frequent in quartz-Fe-dolomite-calcite carbonatite compare to calcite carbonatite. Furthermore, the quartz-Fe-dolomite-calcite carbonatite contains Fe-dolomite (0.4 to 0.5 mm in diameter) that appears in strong association with apatite and anhedral/massive quartz. Pyrochlore only appears in traces and occurs as anhedral to euhedral disseminated crystals (0.2 to 0.4 mm in diameter). Resorbed pyrochlore cores as they occur in calcite carbonatite (Type 1) are absent. Pyrochlore grains show intense patchy zonation (type iii, only present in carbonatite Type 2; 6 C-D) that develops from the grain margins towards the centre and replaces the primary magmatic zonation (type ii). Some pyrochlores, furthermore, exhibit highly porous margins (type iv). In some cases, type iv pyrochlores also form individual grains.

Similar to "common" calcite carbonatites, two types of apatites are identified in quartz-Fe-dolomite-calcite carbonatite. These two types are represented by 1.) individual (anhedral) grains of apatite (Type-III; Fig. 7C) that show a partially resorbed outer rim and internal ovoid zonation (in particular visible by cathodoluminescence microscopy, Fig. 7C), and 2.) massive masses of apatite (Type-IV) that consists of numerous smaller apatite grains (Fig. 7D). While apatite Type-III is typically associated with Fe-dolomite and quartz (Fe-dolomite > quartz), apatite Type-IV (quartz > Fe-dolomite) additionally show a common association with monazite (Fig. 7C–D). Monazite is mostly embedded in quartz (Fig. 3E) but also show large grains that can be found at the contact of calcite and Fe-dolomite (Fig. 3F, G). Comparable to "common" calcite carbonatite, the quartz-Fe-dolomite-calcite carbonatite comprises REE carbonates (bastnäsite, ancylite, and parisite; mostly euhedral with a lath-like appearance) that are frequently in close association with baryte, celestite, and strontianite (usually found in vugs, Figs. 3H, 4H), but also appear as isolated small REE carbonate clusters. Pyrite is rare and typically show altered rims of Fe-hydroxide (Fig. 4I). Minerals formed by post-magmatic mineralization (see Fig. 5) are generally much more abundant in quartz-Fe-dolomite-calcite carbonatite than in "common" calcite carbonatite. Locally, the quartz enrichment swells up as pinkish lenses (Fig. 2C, D). The weathered surface of these lenses appears distinctively uneven and minutely pitted due to resistant quartz with enclosed (less resistant) brown patches of weathered Fe-dolomite (named as parankerite in previous descriptions of Nooitgedacht, Verwoerd, 1967). These lenses also contain massive apatite (Type-V, Fig. 7E), which is similar in appearance to the massive apatite (Type-II) in calcite carbonatite and massive apatites (Type-IV) in quartz-Fe-dolomite-calcite carbonatite. Quartz-Fe-dolomite-carbonatite also contains xenoliths of host rocks (Fig. 2E). In a few cases, remnants of silicate xenoliths (e.g., Nebo granite) are also found in these quartz-rich lenses (Fig. 2C-Small inlier). Usually, however, such xenoliths are completely decomposed and altered, leaving only a mixture of mainly quartz and apatite (±Fe-dolomite) (Fig. 2F).

Type 3 - *Dolomite carbonatite*. Carbonatite type 3 constitutes a brownish porphyritic dolomite dominated carbonatite conformable with the flow structure of the calcite carbonatite, while it occasionally cross cut the same unit (calcite carbonatite). However, it's relation to the quartz-Fe-dolomite-calcite carbonatite is unclear. It almost exclusively consists of dolomite, exhibit disseminated euhedral monazite and pyrite, and contains fragments of quartz (xenocrysts). Calcite is found mostly as microscopic veins along fractures and grain boundaries. No pyrochlore, no apatite and no REE-carbonates has been observed in this carbonatite.

A combined paragenetic sequence including the different carbonatite types of Nooitgedacht is given in Fig. 5.

4.2. Whole-rock geochemistry

The whole-rock major and trace elements data is given in Table 1. Investigated samples (n = 31) are classified according to their dominant carbonate mineralogy (Gittins and Harmer, 1997). This classification is supported by the whole rock geochemistry and classifies carbonatite type 1 (calcite carbonatite) and 2 (quartz-Fe-dolomite-calcite carbonatite) as calcio-carbonatites (n = 26; Fe_2O_3 < 7.41 wt%, MgO <7.17 wt%) and carbonatite type 3 (dolomite carbonatite) as magnesio-carbonatite (n = 4; Fe_2O_3 < 6.10 wt%, MgO 15.4–17.4 wt%). As the quartz-rich lenses (>50 % SiO_2) of quartz-Fe-dolomite-calcite carbonatite represent an important part of carbonatite Type 2, they are additionally listed in the following descriptions and differentiated from the main quartz-Fe-dolomite-calcite carbonatite.

The phosphorous content is 0.05–4.27 wt% for carbonatite Type 1, 1.07–7.31 wt% for Type 2, and 0.11–0.33 wt% for Type 3 carbonatites, while the quartz-rich lens sample (included in carbonatite Type 2) shows 14.1 wt% P_2O_5. The High Field Strength Elements (Zr, Nb, Hf, Ta, Ti, Th) range (in sum) between 8.92 and 1870 ppm for Type 1, 49–90 ppm for Type 2, 31–34 ppm for Type 3, and 11.70 ppm for the quartz-rich lens. The Sr is 144–164 ppm for Type 1, 1603–3164 ppm for Type 2, 1532–3643 ppm for Type 3 and 3884 ppm for the quartz-rich lens. The Ba is 144–164 ppm for Type 1, 144–227 for Type 2, 163–761 for Type 3 while below detection is for the quartz-rich lens.

The ΣREE concentrations in Type 1 carbonatite range between 380 and 1890 ppm, Type 2 carbonatite shows higher ΣREE concentrations between 3000 and 5930 ppm and in Type 3, it ranges between 570 and 2240 ppm. The ΣREE for the quartz-rich lens is 1470 ppm. The REE patterns and trace elements are plotted in Fig. 9A and Fig. 9B, respectively. The carbonatite mineralization discrimination plots (ΣREE vs. Sr/Ba and ΣREE vs. CaO/MgO; Fig. 9C, D) clearly show that calcite carbonatite and dolomite carbonatite plot in the field of barren carbonatites, whereas quartz-Fe-dolomite-calcite carbonatite plots in the "field of mineralized carbonatites" adopted from Hou et al. (2015). The binary plots show the higher silica content from calcite to quartz-Fe-dolomite carbonatite to quartz-rich pink lenses from quartz-Fe-dolomite-calcite carbonatite Fig. 9 E, F.

4.3. Mineral chemistry

4.3.1. Pyrochlore chemistry

The primary niobium phase in carbonatites of the Nooitgedacht Complex are pyrochlore-group minerals (only present in calcite carbonatites and quartz-Fe-dolomite-calcite carbonatites), showing the general formula $A_{2-m}B_2X_{6-w}Y_{1-n}$ (Atencio et al., 2010; Lumpkin and Ewing, 1996; *m, w,* and *n* indicate site vacancies, Zurevinski and Mitchell, 2004; for more details on pyrochlore structure the reader is referred to the cited references). The compositions of investigated pyrochlore group minerals are shown in ES1. Moreover, the mineral maps for selected pyrochlore grains are presented in ES2. The mineral formulae have been calculated based on 2 B site cations. All analyses fall within the pyrochlore subgroup according to the classification of Hogarth (1977; Fig. 6E). According to their textural and compositional specifications pyrochlores at Nooitgedacht can be divided into 4 groups (Fig. 6A–D, A, B):

(i) High AZ (average atomic number; bright in BSE) resorbed cores (Fig. 6A) are defined as oxyuranopyrochlore (after Atencio et al., 2010). The A site is dominated by Ca (1.15 apfu) with low Na (≤0.35 apfu); is relatively enriched in U (up to 0.28 apfu), show moderate REE (up to 0.06 apfu) and a low Th (B.D.L) content. The B-site is relatively enriched in Ta (up to 0.11 apfu), but show low Zr (≤0.02 apfu). Fluorine (≤0.16 apfu, but mostly below detection limit) is low in this pyrochlore type. Nb/Ti (2.46–2.73) is relatively lower than in oscillatory-zoned and patchy pyrochlores but slightly higher than in supergene pyrochlore (see below).

(ii) Primary Oscillatory-zoned pyrochlore is identified as fluorcalciopyrochlore (after Atencio et al., 2010) and predominantly occurs in calcite carbonatite (Fig. 6B, C, D; overprinted in quartz-Fe-dolomite-calcite carbonatite). The A site is rich in Ca (up to 1.11 apfu) and Na (up to 0.87 apfu). Compared to the oxyuranopyrochlore cores, the fluorcalciopyrochlores are much lower in U (B.D.L) and Ta (B.D.L), but have similar REE (up to

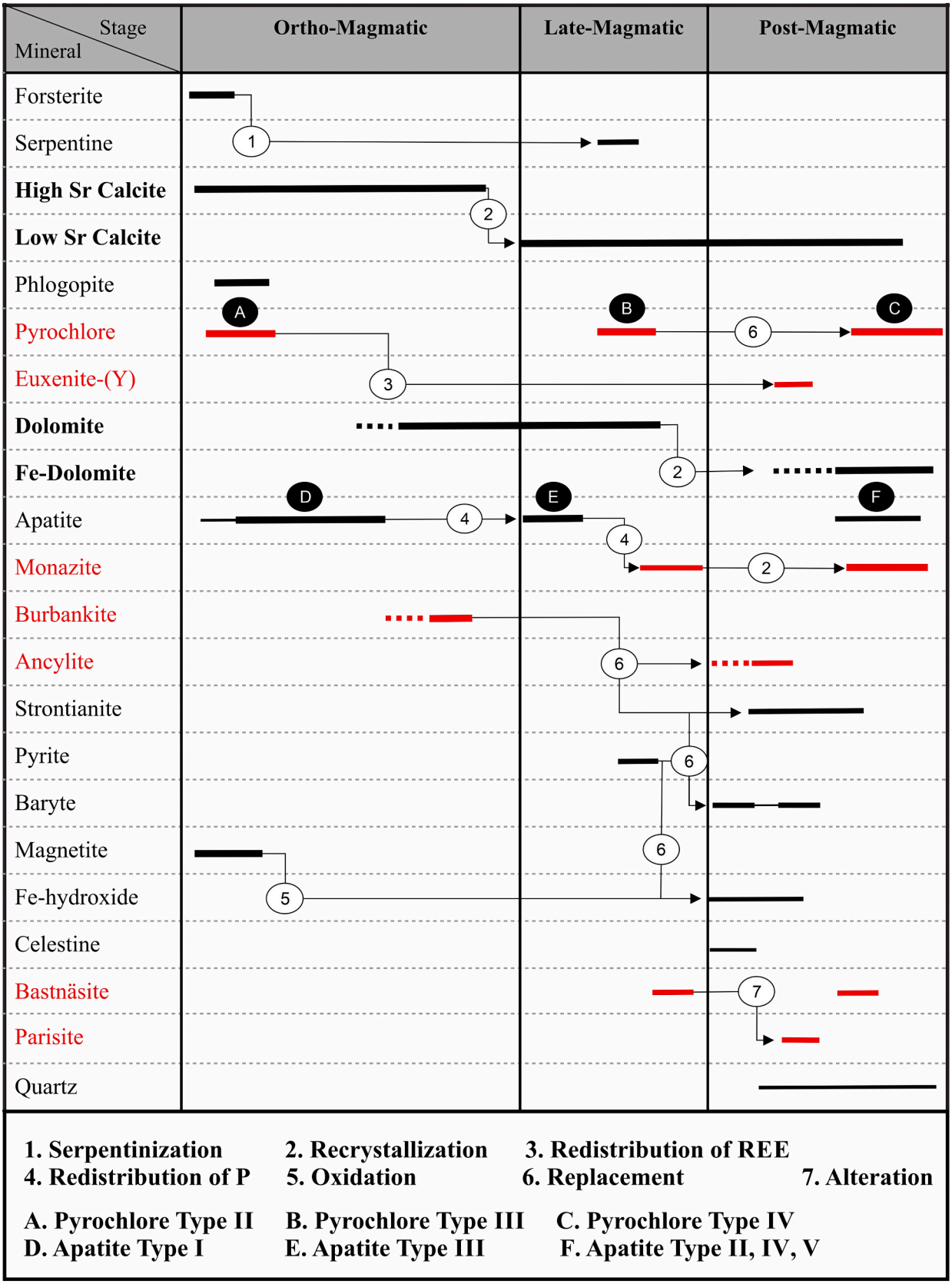

Fig. 5. A detailed paragenetic sequence of calcite-carbonatite and quartz-Fe-dolomite-calcite carbonatite of the Nooitgedacht Carbonatite Complex.

Table 1
Whole rock and trace elements data of Nooitgedacht Complex.

Sample	NDG 01	NDG 05	NDG 5B	NDG 5C	NDG 5D	NDG 5E	NDG 5H	NDG 5I	NDG 5K	NDG 6	NDG 6B	NDG 07	NDG 08	NDG 11	NDG 13	NDG 16	NDG 17	NDG 18	NDG 19	NDG 20	NDG 23	NDG 24	NDG 25	NDG 27	NDG 28	NDG 29	NDG 31	NDG 33	NDG 34	NDG 35	NDG 36
Major elements (wt%)																															
SiO_2	0.091	0.11	0.33	4.60	7.20	bdl	0.70	0.93	5.43	1.09	1.19	4.18	22.28	6.49	0.57	bdl	bdl	0.38	bdl	bdl	3.37	1.04	2.10	0.79	1.00	0.49	0.44	0.67	56.0	1.13	0.57
TiO_2	bdl	bdl	bdl	0.30	bdl	0.073	0.074	bdl	bdl	0.068	bdl	0.062	bdl	bdl	0.26	bdl	bdl	bdl	bdl	bdl	bdl	0.092	bdl	bdl	bdl	bdl	0.061	bdl	bdl	bdl	0.092
Al_2O_3	bdl	bdl	bdl	1.18	bdl	0.071	0.32	bdl	bdl	bdl	bdl	0.31	bdl	0.061	0.053	bdl	bdl	0.10	bdl	bdl	bdl	0.25	bdl	bdl	0.82	bdl	0.073	0.19	bdl	bdl	0.19
Fe_2O_3	0.48	3.41	1.67	4.03	2.06	2.34	5.97	0.77	2.08	1.28	1.93	4.55	1.26	3.74	7.41	0.47	0.30	2.31	0.37	0.48	6.50	6.16	0.77	6.06	3.88	3.07	2.87	2.29	0.57	1.71	3.55
MnO	0.17	0.56	0.45	0.40	0.64	0.66	0.26	0.37	0.59	0.33	0.38	0.64	0.37	0.71	0.22	0.25	0.23	0.23	0.25	0.22	0.57	0.26	0.30	2.14	0.92	0.19	0.16	0.41	0.11	0.23	0.13
MgO	0.95	16.1	15.6	3.99	5.27	4.32	1.30	1.85	4.37	2.69	2.33	7.17	2.41	10.3	1.29	2.02	1.97	1.45	2.51	1.19	0.73	1.32	3.26	17.4	15.4	2.20	1.94	4.99	1.17	4.01	0.68
CaO	51.0	36.2	37.1	46.5	42.5	48.7	46.1	45.3	43.3	47.8	48.4	37.4	36.5	27.4	46.4	49.6	49.3	48.6	43.5	50.8	46.0	46.0	47.2	29.1	34.8	47.9	48.1	45.3	21.3	47.8	49.6
Na_2O	bdl	bdl	bdl	bdl	bdl	bdl	bdl	bdl	bdl	bdl	bdl	bdl	bdl	bdl	bdl	bdl	bdl	bdl	bdl	bdl	bdl	bdl	bdl	bdl	bdl	bdl	bdl	bdl	bdl	bdl	bdl
K_2O	bdl	bdl	bdl	0.16	bdl	bdl	bdl	bdl	bdl	bdl	bdl	bdl	bdl	bdl	bdl	bdl	bdl	bdl	bdl	bdl	bdl	bdl	bdl	0.07	0.12	bdl	bdl	bdl	bdl	bdl	bdl
P_2O_5	bdl	bdl	0.32	0.26	1.22	0.13	4.27	3.89	1.08	0.41	0.057	0.72	7.31	1.07	0.45	0.15	0.084	1.83	bdl	bdl	0.12	1.82	0.18	0.11	1.22	1.61	2.54	0.39	14.1	0.14	2.96
LOI	42.9	40.5	41.2	34.7	38.1	39.4	35.8	43.0	41.6	42.5	42.2	40.3	25.4	46.6	38.7	42.8	42.9	39.9	48.4	41.7	38.2	36.7	41.9	41.7	40.0	38.9	38.0	42.1	3.72	42.3	37.9
SUM	96.3	97.3	96.9	96.2	97.0	95.9	95.5	96.5	98.7	96.4	96.7	95.6	96.0	96.5	96.0	96.1	95.7	95.6	95.9	95.2	95.7	94.6	96.0	97.8	97.7	95.5	95.1	96.6	97.4	97.5	96.0
Trace Elements + Rare Earth Elements (ppm)																															
Li	0.14	0.23	0.35	3.32	0.13	0.076	0.93	0.20	0.15	0.11	0.17	0.38	0.61	0.48	0.22	bdl	0.13	0.57	0.051	0.067	0.25	1.07	0.25	0.37	0.19	0.97	0.53	0.20	0.78	0.29	0.15
Be	0.11	0.22	0.68	0.61	0.35	0.35	0.28	0.42	0.49	0.19	0.24	0.54	0.72	0.86	0.42	bdl	bdl	0.36	bdl	0.092	1.37	0.24	0.14	0.61	0.44	0.072	bdl	0.80	5.45	0.50	0.58
Sc	7.76	16.5	19.2	14.6	12.8	9.69	9.00	16.1	12.7	13.7	12.7	8.98	9.21	20.9	9.50	13.0	12.1	12.5	13.9	8.35	12.1	9.78	17.6	14.9	18.6	7.69	10.4	16.0	2.59	6.24	1.42
V	24.2	14.3	21.2	64.3	32.1	32.0	158.0	11.2	28.2	25.9	22.0	44.4	16.9	22.9	146	19.1	16.8	25.9	19.0	20.6	115	150	15.8	22.7	35.4	66.9	56.7	26.4	2.12	14.8	73.0
Cr	1.03	1.04	1.02	12.8	1.14	1.75	2.10	0.78	1.04	0.52	1.34	3.68	0.76	1.24	0.67	0.33	0.21	0.99	0.40	0.82	13.3	10.4	0.55	18.7	6.04	0.49	0.20	3.38	1.24	0.60	15.9
Co	bdl	bdl	bdl	10.3	4.93	16.3	1.63	bdl	bdl	8.39	5.09	24.7	bdl	3.78	34.2	bdl	bdl	31.3	bdl	5.58	5.95	12.9	bdl	1.94	bdl	10.7	4.22	7.47	bdl	bdl	15.2
Ni	0.92	0.43	2.82	7.79	9.61	6.42	3.43	1.08	1.05	0.68	1.47	2.19	0.63	0.67	0.80	0.30	0.15	11.3	0.25	0.69	10.9	4.41	0.30	7.40	2.22	0.72	0.14	3.07	0.66	0.28	1.57
Cu	5.11	4.97	22.2	42.6	50.7	73.2	2.61	9.14	13.4	6.23	6.54	10.3	9.09	5.00	23.1	1.88	1.18	99.1	2.36	1.94	20.2	4.41	0.71	4.16	1.62	1.26	1.47	5.75	1.56	2.77	9.40
Zn	bdl	21.6	8.90	16.4	5.71	6.94	395.6	3.92	8.39	3.38	1.08	41.5	8.86	19.4	58.0	7.56	1.13	2.29	1.61	5.63	31.6	58.0	bdl	8.61	6.74	120	37.8	3.20	4.99	5.34	29.5
Ga	34.7	17.1	71.2	13.1	106	56.8	60.8	16.9	182	22.2	16.0	55.6	85.6	75.0	27.4	28.6	27.6	34.6	25.5	27.7	52.4	36.6	24.6	30.0	55.1	43.4	53.4	41.0	42.7	36.4	22.2
Rb	0.15	0.075	bdl	5.07	0.064	0.093	0.49	0.057	0.070	0.079	0.091	0.18	0.15	0.27	0.074	0.10	0.066	0.17	bdl	bdl	bdl	1.64	0.19	8.62	1.07	0.52	0.33	0.19	0.17	0.055	bdl
Sr	6199	3643	3122	820	1649	1479	7791	3108	1614	2120	1583	1644	3164	1603	6638	9027	8507	7935	9002	7886	67.0	7269	2178	3066	1532	11,007	9918	1836	3884	776	2978
Y	66.9	12.3	193	19.3	135	43.4	66.7	116	143	48.0	35.1	105	337	84.1	70.7	71.3	69.5	79.1	67.4	74.7	34.5	64.8	39.7	22.4	139	67.6	80.3	113	132	36.9	47.3
Zr	1.47	2.15	4.54	19.0	5.59	1.56	36.9	3.92	5.37	1.74	1.08	11.7	3.1	14.8	2.41	0.31	0.19	0.30	0.60	0.24	5.84	60.5	3.40	6.95	11.3	11.3	61.1	7.61	0.65	4.53	4.8
Nb	4.52	23.6	9.72	18.4	8.84	14.3	619	10.3	4.89	14.3	8.52	16.2	9.63	20.4	34.2	1.21	1.83	15.5	0.51	2.11	8.42	567	23.3	19.6	9.87	23.7	397	36.7	7.40	8.55	0.81
Sb	bdl	bdl	bdl	0.052	0.088	0.14	0.091	bdl	bdl	bdl	bdl	0.11	0.20	bdl	bdl	bdl	bdl	0.076	bdl	bdl	0.34	bdl	0.13	0.075	bdl	bdl	bdl	0.079	bdl	0.057	0.063
Cs	bdl	bdl	bdl	0.29	bdl	bdl	bdl	bdl	bdl	bdl	bdl	bdl	bdl	bdl	bdl	bdl	bdl	bdl	0.083	bdl	bdl	0.11	bdl	bdl	bdl	bdl	bdl	bdl	0.06	bdl	bdl
Ba	483	163	179	321	227	198	651	212	227	209	433	240	144	150	492	531	521	542	530	551	1611	515	1030	736	761	543	569	431	19.1	55.3	458
La	212	124	406	82.1	667	373	287	104	1142	146	119	354	522	596	198	198	191	224	182	197	340	213	178	222	352	270	312	249	243	219	139
Ce	500	269	977	174	1596	861	863	238	2722	328	254	828	1326	1414	485	476	451	543	428	462	840	575	394	513	887	673	781	611	619	557	325
Pr	59.4	31.0	122	20.0	202	104	104	29.2	335	38.7	28.3	102	176	169	58.1	57.5	56.1	71.1	53.2	58.4	114	74.1	47.5	64.0	120	87.6	107	82.6	85.2	75.0	44.9
Nd	222	115	483	73.2	798	407	397	119	1323	145	102	402	752	646	223	216	209	271	198	216	455	277	174	238	489	330	411	338	345	303	176
Sm	36.5	16.3	82.3	10.8	128	62.2	62.7	29.7	188	24.5	15.7	64.6	147	84.4	37.2	36.3	35.1	45.7	33.5	36.3	70.7	45.5	27.9	31.8	82.5	53.4	66.6	63.1	59.8	48.2	28.8
Eu	10.0	3.88	23.3	2.80	34.2	15.5	16.5	10.3	46.0	6.80	4.29	17.9	44.9	19.9	10.3	10.1	9.83	12.5	9.37	10.1	16.5	12.3	7.49	7.37	22.3	14.1	17.7	19.5	16.7	12.3	7.89
Gd	26.1	8.14	60.0	7.06	84.6	36.0	39.5	30.3	103	17.9	11.1	46.0	126	44.8	27.1	26.0	25.7	32.4	24.5	27.0	35.2	30.7	19.1	16.6	54.7	34.7	43.3	50.5	42.5	28.9	20.7
Tb	3.14	0.81	7.95	0.88	9.27	3.27	4.35	4.65	10.2	2.23	1.44	5.69	19.4	4.82	3.30	3.27	3.13	3.85	2.99	3.28	2.90	3.51	2.13	1.54	6.78	3.84	4.78	6.24	5.48	2.87	2.38
Dy	14.8	3.44	40.5	4.30	38.4	12.0	18.5	24.5	40.6	10.8	7.35	26.3	97.0	21.4	15.4	15.5	15.1	17.8	14.3	15.8	10.1	15.8	9.35	6.24	33.6	16.8	20.4	28.7	28.1	11.3	11.1
Ho	2.57	0.56	7.44	0.76	5.86	1.81	2.87	4.43	6.08	1.90	1.38	4.35	15.1	3.46	2.67	2.72	2.63	3.02	2.48	2.79	1.42	2.52	1.53	0.95	5.78	2.66	3.17	4.74	5.10	1.60	1.87
Er	5.93	1.26	17.0	1.72	11.3	3.79	5.72	9.91	11.7	4.43	3.49	8.58	26.9	7.04	6.05	6.22	6.14	6.93	5.85	6.57	3.05	5.49	3.60	1.96	12.8	5.63	6.55	10.5	11.9	3.06	4.17
Tm	0.77	0.16	2.06	0.21	1.19	0.48	0.65	1.22	1.27	0.59	0.50	0.87	2.65	0.79	0.77	0.80	0.80	0.86	0.75	0.84	0.38	0.64	0.50	0.23	1.48	0.63	0.73	1.27	1.37	0.32	0.50
Yb	4.21	0.86	9.84	1.12	5.40	2.53	3.22	6.37	5.83	3.42	2.95	3.64	11.4	3.87	4.14	4.44	4.43	4.69	4.15	4.71	2.15	3.42	3.10	1.20	6.99	3.16	3.58	7.1	6.40	1.58	2.64
Lu	0.62	0.12	1.26	0.16	0.65	0.33	0.45	0.88	0.74	0.52	0.46	0.44	1.40	0.52	0.61	0.65	0.64	0.68	0.60	0.69	0.31	0.48	0.49	0.17	0.91	0.44	0.50	0.99	0.77	0.22	0.38
Hf	0.10	0.089	0.29	0.51	0.28	0.087	0.47	0.21	0.31	0.087	0.060	0.31	0.55	0.37	0.17	0.086	0.10	0.12	0.10	0.10	0.17	0.88	0.12	0.16	0.38	0.21	0.98	0.40	0.18	0.21	0.10
Ta	bdl	bdl	0.083	0.16	0.053	0.23	0.29	0.075	bdl	0.089	0.091	0.16	0.11	0.18	0.13	bdl	bdl	bdl	bdl	bdl	0.074	0.24	0.21	bdl	0.073	bdl	16.0	0.069	bdl	bdl	0.13
W	0.23	1.55	0.75	0.60	0.34	0.56	0.32	0.61	0.52	0.68	0.25	1.10	2.37	0.80	0.26	1.41	0.54	0.27	1.06	0.24	1.47	0.19	0.44	0.35	0.44	0.17	0.28	0.14	13.4	4.78	0.65
Pb	5.83	4.41	7.52	3.94	5.15	15.1	63.9	3.93	8.32	3.01	4.28	17.43	14.1	4.06	5.18	5.12	4.9	5.69	4.79	5.80	3.11	23.9	3.01	3.38	2.50	22.1	43.1	9.82	5.91	1.82	3.30
Bi	bdl	bdl	bdl	0.092	bdl	bdl	1.48	bdl	bdl	bdl	bdl	0.059	bdl	bdl	bdl	bdl	bdl	bdl	bdl	bdl	bdl	0.12	bdl	bdl	bdl	0.40	0.18	0.20	bdl	bdl	bdl
Th	2.82	7.09	20.7	5.09	34.8	29.8	149	4.69	53.7	5.01	5.43	45.8	77.2	14.8	5.72	0.26	0.54	6.21	0.12	0.44	8.44	156	2.94	4.61	12.4	99.8	302	21.6	3.55	5.21	17.1
U	0.084	0.33	3.43	0.24	0.19	0.10	1.19	0.39	0.15	0.52	0.16	0.31	0.75	0.44	0.18	bdl	0.13	1.13	bdl	0.076	3.46	2.75	1.02	0.86	0.74	3.19	391	3.96	0.38	0.29	0.73
TREE	1098	574	2239	379	3582	1883	1805	613	5934	731	553	1865	3269	3015	1072	1054	1012	1238	959	1041	1891	1259	869	1106	2077	1496	1778	1473	1470	1265	765

bdl = below detection limit, TREE = Total Rare Earth Elements.

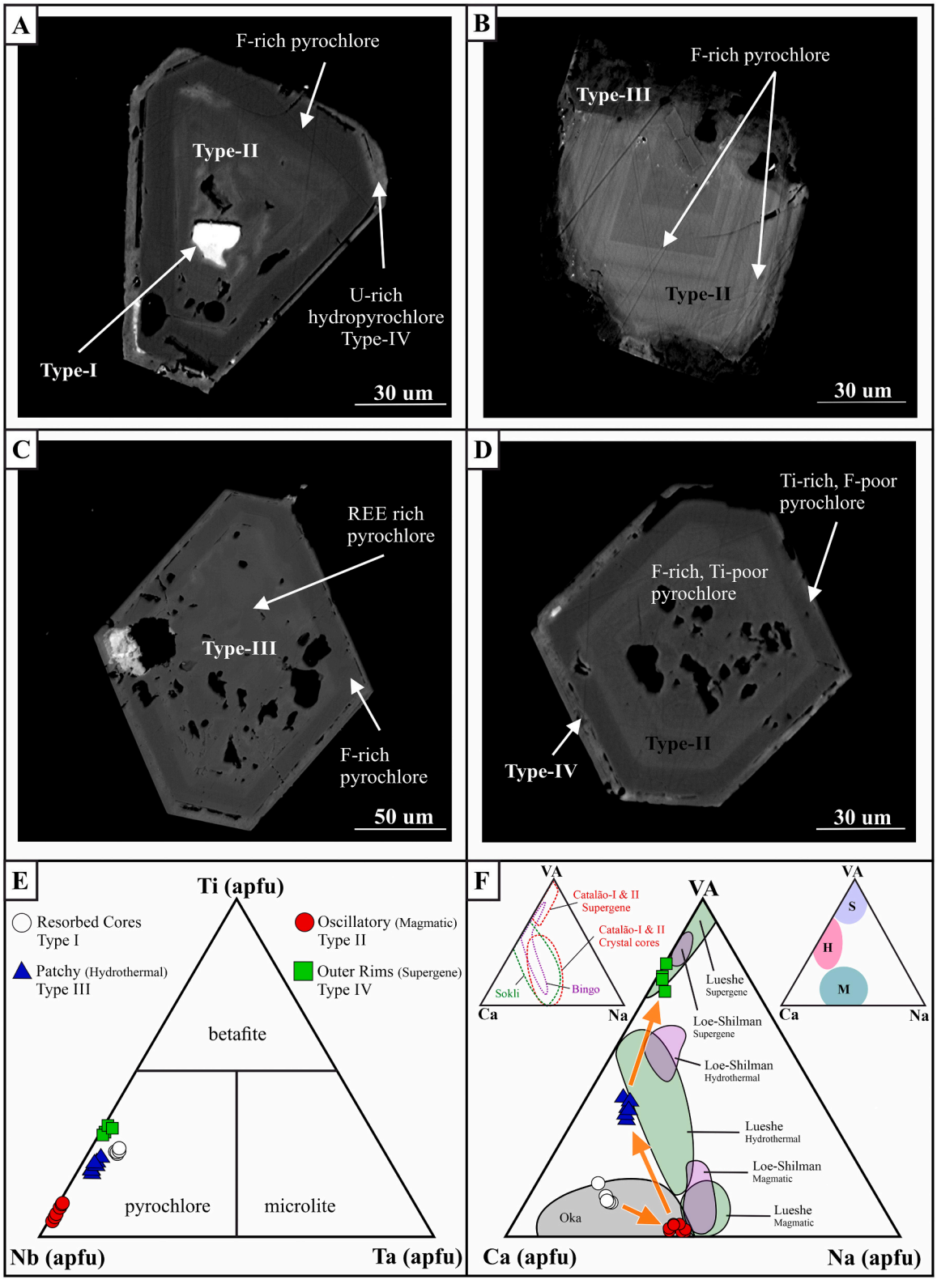

Fig. 6. Textural and compositional variations of pyrochlore of the Nooitgedacht complex. (A) Pyrochlore with bright BSE core (U-Ta rich) surrounded by magmatic oscillatory F-rich pyrochlore. Some patchy REE-rich zonation is visible. The outer rim is Uranium-Cerium rich. (B) Oscillatory zonation in pyrochlore with F-rich zones. The outermost part has been altered by hydrothermal fluids. (C) Primary F-rich pyrochlore altered by fluid overprint, preserved as patchy zonation (REE-rich). (D) Primary magmatic oscillatory zones pyrochlore (type II). Zonation shows differences in F and Ti content. (E) Ti-Nb-Ta ternary diagram showing the composition of pyrochlores. The outer U-Ce rich rim is also visible (Type-IV), (F) Na-Ca-VA ternary diagram showing the compositional evolution of pyrochlore in the Nooitgedacht Complex. For comparison, pyrochlore of other complexes is plotted: Oka (Gold, 1986; Zurevinski and Mitchell, 2004), Sokli (Lee et al., 2006), Lueshe (Nasraoui and Bilal, 2000), Bingo (Williams et al., 1997), Loe-Shilman (Khan et al., 2021) and Catalão I and II (de Oliveira Cordeiro et al., 2011; Guarino et al., 2017). M = magmatic, H = hydrothermal, and S = supergene fields (after Zurevinski and Mitchell, 2004). (For interpretation of the references to colour in this figure legend, the reader is referred to the web version of this article.)

0.03 apfu), Zr (up to 0.01 apfu) and Th (B.D.L) contents. Fluorine tends to be higher (0.91–0.98 apfu). Niobium/Titanium (8.90–15.58) is highest among all other pyrochlore groups at Nooitgedacht.

(iii) Patchy-zoned pyrochlore (Fig. 6C) is defined as hydroxycalciopyrochlore (after Atencio et al., 2010). The A site of this group of pyrochlore is relatively low in Ca (≤0.75 apfu), generally low in Na (≤0.19 apfu), and characterized by a markable A site vacancy (*m*). A and Y site vacancies increase with low-

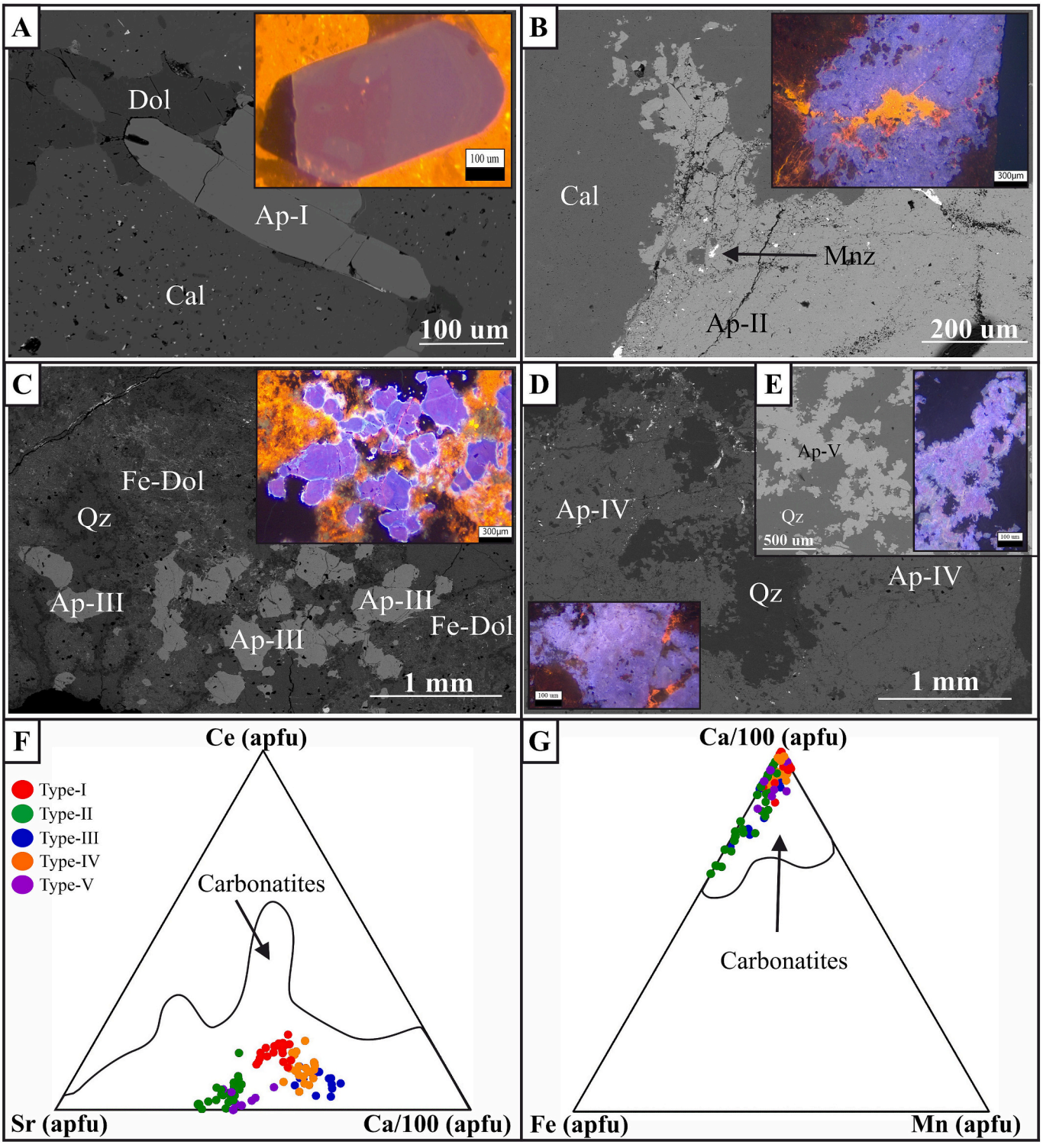

Fig. 7. Textural and compositional variations of apatite from the Nooitgedacht Carbonatite Complex. (A) Pill shaped primary apatite (type-I) in calcite carbonatite. An oscillatory zonation is obvious in the CL image inlier. (B) Massive/hydrothermal apatite (type II) in calcite carbonatite. (C) Internally ovoidal-zoned apatite (type III) in quartz-Fe-dolomite-calcite carbonatite. (D) Massive/hydrothermal apatite (type IV) in quartz-Fe-dolomite-calcite carbonatite. (E) Massive/hydrothermal apatite (type-V) in a quartz-rich lens. (F) Ce-Sr-Ca/100 (apfu) ternary diagram for apatite classification. (G) Ca/100-Fe-Mn ternary diagram. Both, Fig. F and G shows that all apatites from the Nooitgedacht Carbonatite Complex fall into the defined field of carbonatites (after Teiber et al., 2015).

temperature alteration (Lumpkin and Ewing, 1996; Wall et al., 1996). Uranium (up to 0.11 apfu) and Th (up to 0.11 apfu), reach higher contents than in the oscillatory-zoned fluorcalciopyrochlores, but lower contents than in resorbed cores of oxyuranopyrochlore. Zirconium (up to 0.18 apfu), REE (up to 0.21 apfu) and Ta (up to 0.05 apfu) reach higher contents than in resorbed cores of oxyuranopyrochlore and oscillatory-zoned fluorcalciopyrochlores. Fluorine ranges between 0.04 and 0.08 apfu, which is higher than in weathered pyrochlore (group iv), while lower than in oscillatory pyrochlores and most resorbed cores. Niobium/Titanium (3.02–3.97) is slightly higher than in resorbed cores and weathered pyrochlores while lesser than in oscillatory-zoned pyrochlores.

(iv) Weathered/secondary-replaced pyrochlore forming outer rims around other pyrochlores (and form few discrete grains of this group) and correspond to hydropyrochlore (Fig. 6A, D). A prominent vacancy at the A site ranges from 0.80 to 1.0 apfu, Ca and Na (combined 0.01–0.27 apfu) occupancy is accordingly low. The F content tends to zero. The U content, in contrast, is typically increased to 0.17–0.2 apfu. REE is highest in this pyrochlore group, with up to 0.29 apfu; Zr is 0.03–0.05 apfu, Ta is ~0.02 apfu, and Th is ~0.01 apfu. Niobium/Titanium is 1.98 to 2.23, which is the lowest Nb/Ti value among all pyrochlore groups.

4.3.2. *Apatite chemistry*

Representative analyses of apatite are presented in ES1, and formula recalculations (based on $Ca_{10}(PO_4)_6(F, OH)_2/M_{10}(XO_4)_6Z_2$) were performed using the method of Ketcham (2015). Apatites of the Nooitgedacht carbonatites depict characteristics typically seen in carbonatites, as described by Chakhmouradian et al. (2017). As common for apatites from carbonatites (Teiber et al., 2015; Fig. 7F, G), the Cl content (<0.02 apfu) of all apatite types at Nooitgedacht is very low. Na is also relatively low in all apatites (0.018–0.057 apfu) and forms a compositionally undifferentiable cloud, without any correlation or tendency. However, due to their compositional (and textural) differences apatites of Nooitgedacht carbonatites can be grouped into 5 different types of apatite

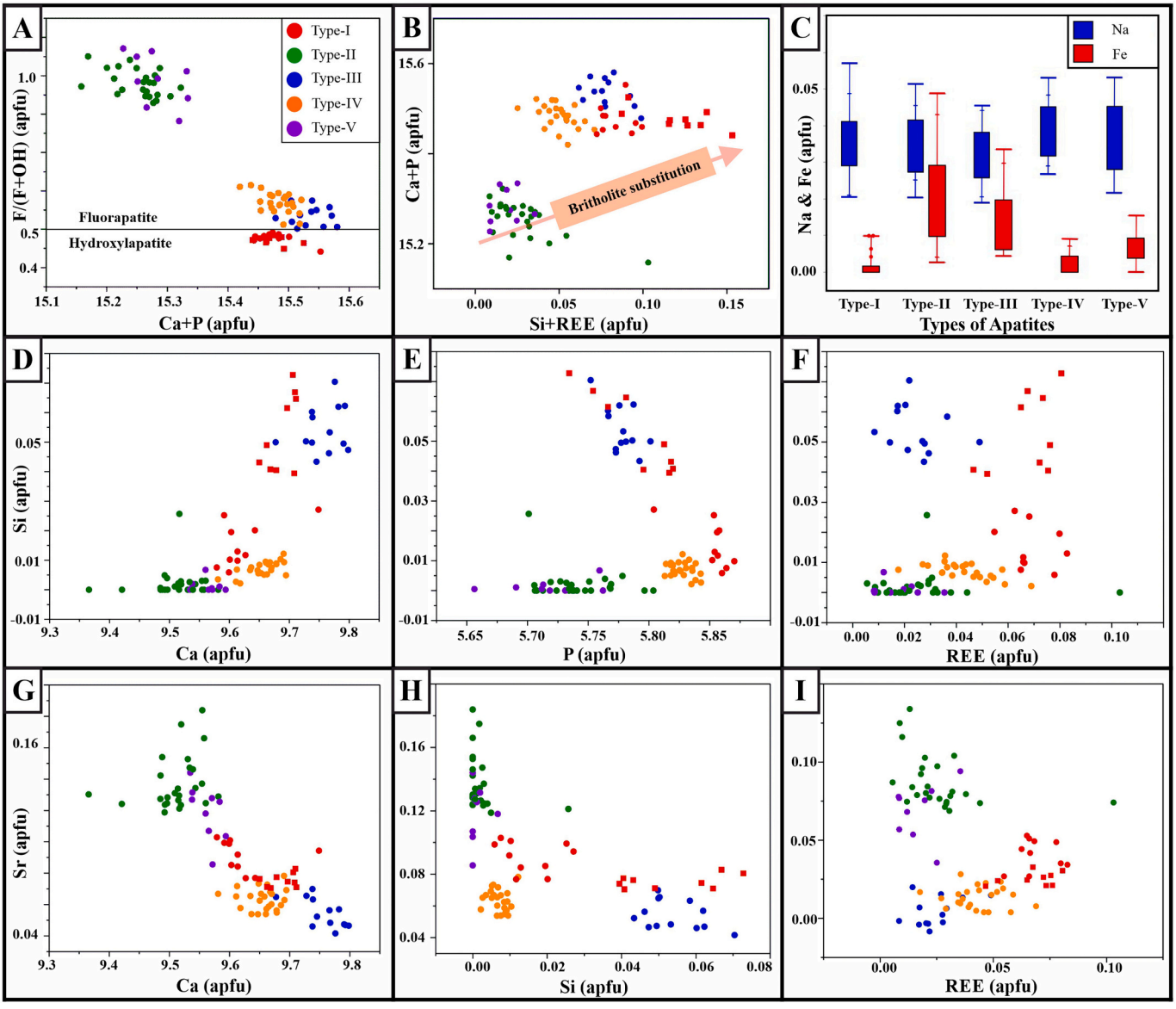

Fig. 8. Binary plots of the various types of apatites from the Nooitgedacht Carbonatite Complex. (A) Ca + P vs. F/F + OH. (B) Si + REE vs. Ca + P. The arrow follows the britholite substitution. (C) Box plots show the Na and Fe contents of apatites. (D), (E), and (F) Si (y-axis) vs Ca, P, and REE, respectively. (G), (H), and (I) Sr (y-axis) vs Ca, Si, and REE, respectively. Please note that the red dots represent core of apatites while red box shows rim. (For interpretation of the references to colour in this figure legend, the reader is referred to the web version of this article.)

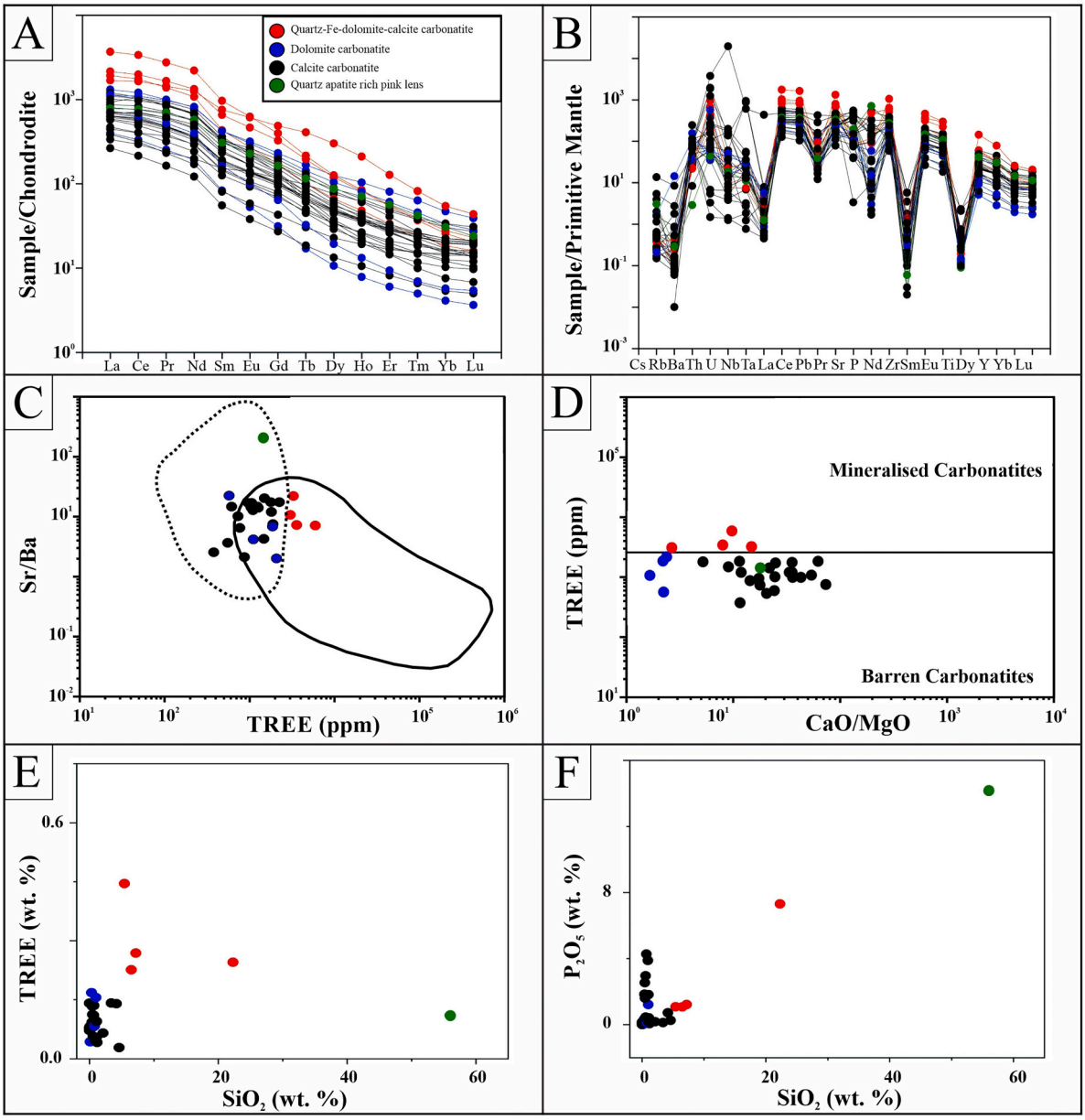

Fig. 9. Whole rock geochemical plots of the Nooitgedacht carbonatites. (A) Chondrite normalized REE Patterns (after McDonough and Sun, 1995) showing enrichment of REE in more evolved quartz-Fe-dolomite-calcite carbonatites. (B) Primitive Mantle spider diagram (after McDonough and Sun, 1995). U, Nb and Th content is higher in the calcite carbonatites (this correlates with mineral abundance and mineral chemistry of pyrochlore). Depletion in Zr is typical for carbonatites. (C) REE (ppm) vs. Sr/Ba plots showing barren vs. mineralized compositions. Quartz-Fe-dolomite-calcite carbonatites fall into the mineralized carbonatite zone (dotted line marks barren, solid line fertile carbonatites). (D) Quartz-Fe-dolomite-calcite carbonatites fall into the mineralized carbonatites field. (E) SiO_2 vs. TREE (wt%) binary plot shows the higher TREE and SiO_2 content in quartz-Fe-dolomite-calcite carbonatite. (F) SiO_2 vs. P_2O_5 binary plot shows a positive trend from calcite carbonatite to quartz-Fe-dolomite-calcite carbonatite, to the quartz-rich lenses (in respect to the enrichment of silica and phosphate).

(Fig. 8A–I):

Apatite type I (prismatic/pill shaped): The pill shaped apatites are classified as hydroxyapatites (Fig. 8A) (exceptional for apatites of the Nooitgedacht complex) with an F content ranging from 0.88 to 0.98 apfu. In comparison to the other apatite types, type I apatite shows the highest concentrations of REE (up to 0.08 apfu), while the Sr content is immediate (0.07 to 0.1 apfu). Type I apatites demonstrate the widest range of P and Si (5.73–5.87 and 0.006–0.07 apfu, respectively), with a good negative correlation between both, which points to britholite substitution ($Ca^{2+} + P^{5+} \leftrightarrow REE^{3+} + Si^{4+}$) (Fig. 8B). However, a positive correlation of REE with increasing Si is not directly observed. Due to their P and Si contents compositions of type I apatites cluster in two subgroups. Both subgroups differ particularly in their Ca, Si and P contents. Subgroup Ia (high P, low Si, relatively low Ca) reflects analyses of cores of apatite type I, while subgroup Ib (intermediate P and Ca, relatively high Si), which resembles the composition of apatite type III (regarding P, Si, Ca contents), represents rims of apatite type I. Fe (<0.01 apfu) is generally low in apatite type I (Fig. 8C).

Apatite type II (massive): Apatite type II is classified as fluorapatite (Fig. 8A). The F content ranges from 1.66 to 1.89 apfu. These apatites (together with type V) exhibit the highest F content in apatites of Nooitgedacht. REE in type II reflects relatively low concentrations (0.01–0.04 apfu) and span the same range as apatite types III and V, with strong overlaps to type IV. Sr content in apatite II (0.12–0.18 apfu) is the highest among all apatites types. P (5.7–5.8 apfu) and Si (<0.004 apfu), both show the lowest content in comparison with the other apatite types

(except type V). The deficit (0.2–0.3 apfu) on the tetrahedral PO_4-position indicates a potential occupation of the X-site by an additional component, most likely CO_3^{2-} or OH (e.g., Anenburg et al., 2024). Ca (9.5–9.6 apfu) in apatite type II is lowest among all apatite types. Although they occur in different rocks, apatite types II and V almost always follow the same chemical composition/trends. Only the Sr content is in average slightly higher and the Fe content (0.002–0.5 apfu) is noticeable higher (similar to type III) in apatite type II. The group of type II and V is chemically clearly separate from the other apatites.

Apatite type III (individual grains with ovoid zonation): Apatite type III is classified as fluorapatite, as well (Fig. 8A). The F content ranges from 1.0 to 1.15 apfu. The REE concentration is low (0.01–0.05 apfu) and the Sr content (0.04–0.07 apfu) is the lowest among apatites of Nooitgedacht. While P content is immediate (5.75–5.8 apfu), the Si (0.04–0.07; together with subgroup Ia) and Ca contents (9.7–9.8) are the highest. In comparison to the other apatite types (except type II) type III show elevated concentrations of Fe (0.004–0.033 apfu).

Apatite type IV (massive): Apatite type IV is classified as fluorapatite, with F ranging from 1.55 to 1.94 apfu. REE concentration is intermediate (0.02–0.07 apfu) and Sr relatively low (0.05–0.08 apfu). Phosphorous is high (5.81–5.84), Si is low (0.012–0.002 apfu) and Ca show intermediate values (9.58–9.69 apfu). Fe is generally low (<0.01 apfu). In most cases, the composition of type IV apatites lies between apatite type I and III.

Apatite type V (massive): As stated above, the composition of fluorapatite type V (F = 1.02–1.23, REE = 0.01–0.03, P = 5.7–5.76, Si < 0.007, Ca = 9.53–9.6 apfu), almost completely reflects the composition of type II. Only Sr (0.08–0.14 apfu) of type V is slightly lower and the Fe content (<0.015 apfu) is in average noticeable lower than that of type II.

As the compositional characteristics of the individual apatite types has already shown, the apatite types of Nooitgedacht can be basically divided into two clusters (Fig. 8A). Cluster 1 includes apatite types I, III and IV, and cluster 2 includes type II and V. Cluster 1 show different common inter-elemental correlations (e.g., Ca vs. REE, Sr vs. REE, Ca vs. P), while cluster 2 separates as an irregular cloud often shifted from the compositional tendencies of cluster 1. In particular, the plot P against Si clearly demonstrates the difference between the two clusters. While in cluster 1 Si correlates negatively with P, cluster 2 shows (at permanently low Si concentrations) no correlation with P. Furthermore, the F content clearly separates both clusters. Common tendencies in contrast are given by the negative correlation between Sr and Si (mirrored to the positive correlation between Ca and Si). The Sr content generally decreases in a common trend from apatite types II > V > III > I > V.

4.4. Raman spectroscopy

Apatites of all types from calcite carbonatite and quartz-Fe-dolomite-carbonatite were used for Raman spectroscopy. Strong, typical bands of apatite were observed at 970 cm^{-1} for all types of apatites (ES2). A strong OH peak for type-I apatites were observed at around 3200–3300 cm^{-1}.

Although CO_3^{2-} groups are very likely in particular for apatite type II and V (see above), Raman spectroscopy on the corresponding apatites did not prove conclusive with regard to the X-site deficiencies ES2. However, earlier work had already concluded that apatites with very small deficits and potential other substituent elements at this site in particular do not give good results on the identification of CO_3^{2-} groups (e.g., Chakhmouradian et al., 2017).

4.5. U-Pb dating

Apatites (and pyrochlore) from calcite carbonatite and quartz-Fe-dolomite-calcite carbonatite were selected for in situ U-Pb dating. Due to the unavailability of apatite and pyrochlore, no age data was produced for dolomite carbonatites. Age dating of apatite type I (n = 23), apatite type II (n = 38), and pyrochlore type ii (n = 22) from calcite carbonatite (carbonatite type I) resulted in an age of 1328.9 ± 13.3/19.7 Ma, 1324.2 ± 8.5/16.8 Ma and 1334.1 ± 15.2/21.0 Ma, respectively (Fig. 10A, B, C). The combined consideration of the data shows a good match between ca. 1340 Ma and 1310. Age dating of apatite type III (n = 36) from quartz-Fe-dolomite-calcite carbonatite, in contrast, resulted in an age of 1279.2 ± 11.6/18.2 Ma (Fig. 10D). This age differs notably (within error limits) from the age estimated for calcite carbonatite. Due to low U contents in apatite type IV and V (Uranium did not exceed the threshold required for appropriate age dating), it was not possible to determine the age for these apatites.

4.6. Stable carbon-oxygen isotopy

Seventeen (calcite carbonatite: n = 9; quartz-Fe-dolomite-calcite carbonatite: n = 4; and dolomite carbonatite: n = 4) whole rock samples were analysed for carbon and oxygen isotopes of carbonates. The results are presented in Table 2. The values for calcite carbonatites range between 7.64 and 9.89 ($\delta^{18}O$) and −4.01 to −4.61 ($\delta^{13}C$). For quartz-Fe-dolomite-calcite carbonatite $\delta^{18}O$ and $\delta^{13}C$ show 11.3 to 13.3 and −2.02 to −2.65, respectively. Dolomite carbonatite exhibits values of 10.2 to 12.9 ($\delta^{18}O$) and −1.96 to −3.16 ($\delta^{13}C$). All calcite carbonatite samples lie within the primary igneous carbonatite box (Taylor et al., 1967), while quartz-Fe-dolomite-calcite carbonatites and dolomite carbonatites plot outside the box, following the path for crustal contamination and/or high temperature fractionation (Fig. 11).

5. Discussion

5.1. Pyrochlore as a monitor of carbonatite evolution/alteration

The mineral chemistry of pyrochlore is fairly variable. In particular in carbonatitic rocks, a specific pyrochlore composition may typically decipher distinct processes within the magma/rock evolution (e.g., Chakhmouradian and Mitchell, 1998; Khromova et al., 2017; Lee et al., 2006; Lottermoser and England, 1988; Nasraoui and Bilal, 2000; Walter et al., 2018; Zaitsev et al., 2012, 2021; Zurevinski and Mitchell, 2004; Jago and Gittins, 1993; Lumpkin and Ewing, 1996; Viladkar and Sorokhtina, 2021; Benkó et al., 2021; Khan et al., 2021; de Oliveira Cordeiro et al., 2011). Pyrochlore crystallization in carbonatites is a complex process that can occur through various processes including magmatic and post-magmatic alteration processes. Although direct magmatic crystallization is more common especially in an alkali-rich environment at high Ca activity and 600 °C, prior studies suggest that pyrochlore may also originate or undergo modification via interactions between carbonatite magma and adjacent rocks (Viladkar and Sorokhtina, 2021; Vasyukova and Williams-Jones, 2023). Similarly, during the ascent of carbonatite melt and reaction with crustal lithologies, additional elements can be introduced to the melt, that can potentially influence the pyrochlore composition. Additionally, the transition from carbonatite melt to a fluid-rich system in the late stages (300 °C) can modify the primary magmatic pyrochlore composition (from REE-poor to REE-rich pyrochlores; Viladkar and Sorokhtina, 2021; Vasyukova and Williams-Jones, 2023).

Pyrochlore enriched in U and/or Ta is typically formed in syenitic magmas (e.g., Lueshe carbonatite, Congo; Nasraoui and Bilal, 2000; Mariupol Massif, Ukraine; Dumańska-Słowik et al., 2014; Nosean syenites from Kaiserstuhl Volcanic Complex, Germany; Walter et al., 2018). It is therefore suggested that partially disintegrated U and Ta-rich pyrochlore cores, which are found in carbonatites, represent inherited relict pyrochlores originally derived from spatially associated syenites (e.g., Lueshe carbonatite, Congo; Nasraoui and Bilal, 2000 and Kaiserstuhl Volcanic Complex, Germany; Walter et al., 2018). Pyrochlore cores (oxyuranopyrochlore) of corresponding composition (and texture) discovered at Nooitgedacht are accordingly suggested to have crystallized in a silicate (syenitic) magma. These pyrochlores might be dragged into the carbonatite magma, and got fractured and/or partially resorbed

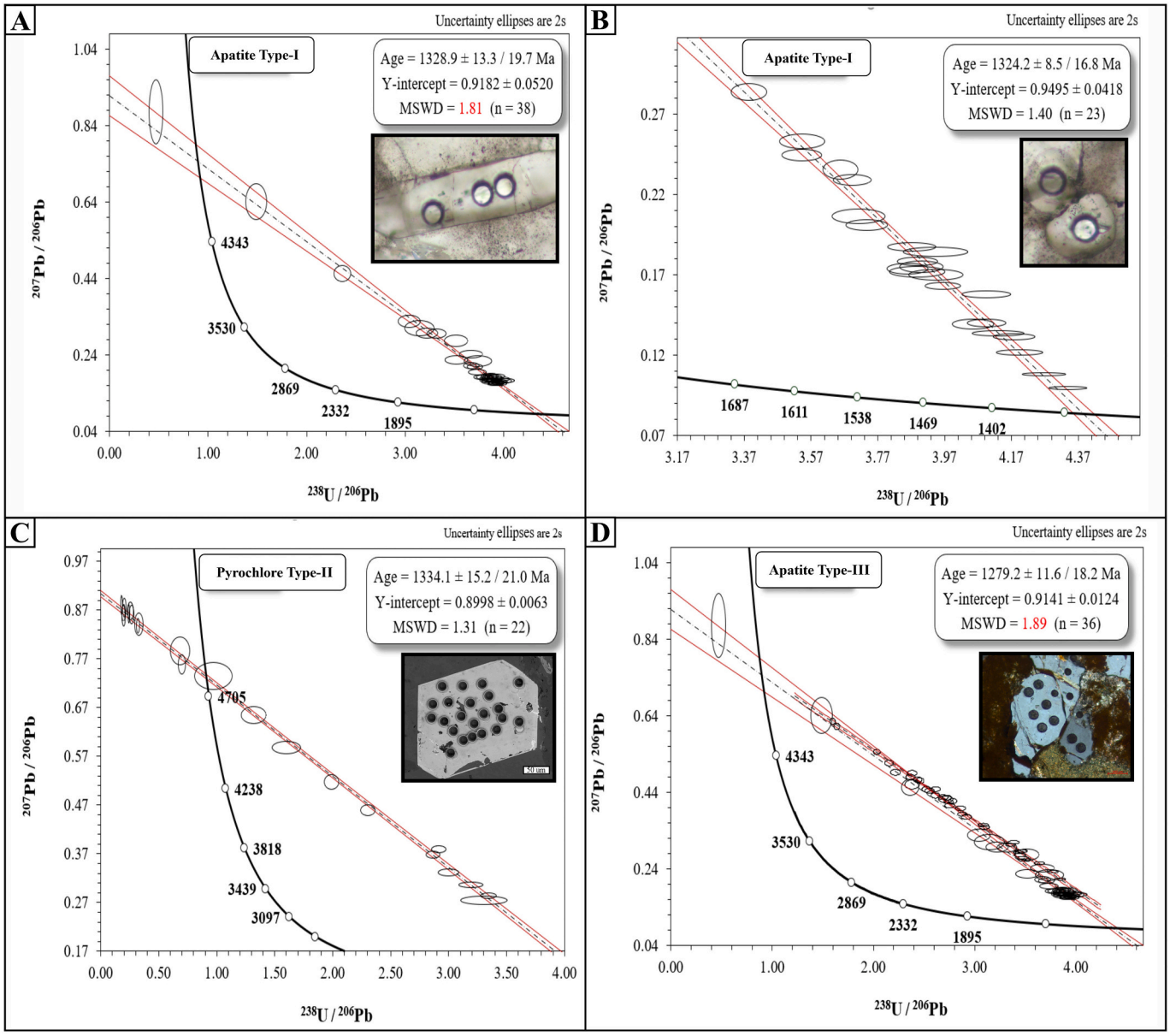

Fig. 10. Tera-Wasserburg plots of apatite and pyrochlore from the Nooitgedacht Carbonatite Complex. (A, B) Tera-Wasserburg plots reflecting pill shaped apatites (type I) from calcite carbonatites. (C) Tera-Wasserburg plots reflecting magmatic pyrochlore (type-II) from calcite carbonatite. (D) Tera-Wasserburg plots reflecting ovoidal-zoned apatites (type-III) from quartz-Fe-dolomite-calcite carbonatite. The black circles show the laser spots.

during magma ascent and subsequent emplacement. Fluorine-enriched pyrochlores, in contrast, are suggested to be most likely crystallized directly from a carbonatite magma (e.g., Chakhmouradian, 2006; Mitchell and Liferovich, 2005; Zurevinski and Mitchell, 2004), while in particular the formation of oscillatory zoning (in pyrochlore) is distinctively attributed to magmatic crystallization (Hogarth et al., 2000; Walter et al., 2018). Oscillatory-zoned F-enriched pyrochlores (fluorcalciopyrochlore; occasionally overgrowing inherited U/Ta-rich pyrochlore cores; (Fig. 6A) of Nooitgedacht carbonatites are accordingly assigned to the ortho-magmatic stage. Fluorine-poor compositions of pyrochlore (in carbonatitic systems), on the other hand, are indicative for a hydrothermal formation (Bambi et al., 2012). Furthermore, the presence of vacancies in the A-site of the pyrochlore structure reveal a general alteration. Corresponding pyrochlores often experienced fracturing and dissolution. The extent of vacancies/defects increase significantly from late-stage hydrothermal alteration to low-temperature subsurface weathering. Lumpkin and Ewing (1996), and Wall et al. (1996) comprehensively examined this phenomenon. Vacancies, occasionally associated with Si, Sr, Ba, Th and/or REE-enrichment, are ascribed to hydrothermal alteration at Sokli (Lee et al., 2006), hydrothermal overprint at Oka (Zurevinski and Mitchell, 2004), Lueshe (Nasraoui and Bilal, 2000), Bingo carbonatite (Williams et al., 1997), Loe-Shilman (Khan et al., 2021), and Catalão-I (de Oliveira Cordeiro et al., 2011) (Fig. 6F). Fluorine-poor pyrochlore (A-site vacancy 0.50–0.60 apfu; hydroxycalciopyrochlore) of Nooitgedacht is accordingly interpreted as a result of hydrothermal overprinting, while almost F-free pyrochlore (A-site vacancy 0.81–1.00 apfu; hydropyrochlore) of Nooitgedacht is considered to be the product of weathering (Fig. 6F). Consequently, the different types of pyrochlore identified in the carbonatites of Nooitgedacht show an evolutionary path from a magmatic through hydrothermal to supergene formation. Based on Na and Ca content and A-site vacancy, the different groups and corresponding formation processes can be clearly distinguished in Fig. 6F. While some authors do not distinguish between the different groups of pyrochlores

Table 2
C-O isotope analysis of the Nooitgedacht Carbonatite Complex.

Sample	δ18O V-SMOW	δ13C V-PDB	Type
NDG-5D	12.1	−2.28	Quartz-Fe-Dolomite-Calcite Carbonatite
NDG-5B	10.3	−2.59	Dolomite Carbonatite
NDG-5 K	7.72	−4.32	Calcite Carbonatite
NDG-17	7.64	−4.36	Calcite Carbonatite
NDG-19	7.69	−4.31	Calcite Carbonatite
NDG-20	7.81	−4.38	Calcite Carbonatite
NDG-11	11.5	−2.03	Quartz-Fe-Dolomite-Calcite Carbonatite
NDG-5 K	11.3	−2.29	Quartz-Fe-Dolomite-Calcite Carbonatite
NDG-5H	9.90	−4.18	Calcite Carbonatite
NDG-18	8.92	−4.30	Calcite Carbonatite
NDG-16	9.23	−4.36	Calcite Carbonatite
NDG-8	13.4	−2.66	Quartz-Fe-Dolomite-Calcite Carbonatite
NDG-5	9.11	−3.16	Dolomite Carbonatite
NDG-28	12.9	−1.96	Dolomite Carbonatite
NDG-27	11.7	−2.84	Dolomite Carbonatite
NDG-29	7.94	−4.61	Calcite Carbonatite
NDG-31	7.91	−4.61	Calcite Carbonatite

in their studies (pyrochlores are summarized in big clusters), the present study (with reference to further detailed pyrochlore studies; e.g., references cited in Fig. 6F) shows that a clear distinction is feasible.

5.2. Magmatic vs. hydrothermal apatite

Systematic variations in apatite composition may characterize changing conditions during the successive crystallization of apatite during carbonatite emplacement (Chakhmouradian et al., 2017; Walter et al., 1995). In particular, core-rim variations may indicate a shift in crystallization conditions. In general, all analysed apatites exhibit the typical composition for apatite formed in carbonatites (Fig. 7F, G; Teiber et al., 2015). The comprehensive review of apatite composition in carbonatitic environments by Chakhmouradian et al. (2017) emphasizes that apatite in carbonatites typically form Cl-poor fluorapatite and F-rich-hydroxylapatite (≥0.6 F pfu in respect to $Ca_{10}(PO_4)_6(F, OH)_2$). Apatites analysed in the present study (0.88–1.93 F pfu; <0.02 Cl pfu) nearly completely fill this range of apatite composition. Considering the F content of all apatites, a tendency towards successive enrichment of F during the evolution of apatites from the ortho-magmatic to the hydrothermal stage becomes evident. A distinction between magmatic and hydrothermal apatites is primarily based on the textural appearance as pill-shaped and ovoid apatites (magmatic; apatite type I and III, respectively) and interstitial masses (hydrothermal; apatite type II, IV and V). Magmatic apatites (type I) of the first carbonatite intrusion are F-rich-hydroxylapatites, while both, hydrothermal apatites (type II) of carbonatite type 1 and apatites (type V) of the quartz-rich lenses show the highest F contents with almost complete occupation of the X-site by F. A considerable enrichment of F in hydrothermal apatites has already been reported by Chakhmouradian et al. (2017). They further point out the depletion of REE in hydrothermal apatite and a typical enrichment of REE in magmatic apatites, which can similarly be observed in the apatites of Nooitgedacht. Although the apatites of Nooitgedacht generally exhibit very low REE contents, the magmatic apatites (type I) show the highest REE values (0.05–0.08) among these low concentrations. The most prominent coupled substitutions that result in the incorporation of REE into apatite are the britholite ($Ca^{2+} + P^{5+} \leftrightarrow REE^{3+} + Si^{4+}$) and belovite ($3Ca^{2+} \leftrightarrow REE^{3+} + Na^{+} + Sr^{2+}$) substitutions. While a distinct Si incorporation in apatite rather assigned to ortho-magmatic conditions, the incorporation of Na is considered to be related to late crystallization in a residual melt or hydrothermal conditions (at relatively low temperatures; Giebel et al., 2019b and references therein). The pill-shaped apatite reveals a weak Si incorporation in its rims (0.03–0.07 apfu; apatite type Ib). This Si enrichment is very similar to the Si enrichment of the primary apatites (0.04–0.07 apfu; type III) of the second generation of carbonatites (quartz-Fe-dolomite-calcite-carbonatite). But there are also clear differences (e.g., in REE, F and Sr content). However, a direct relationship cannot be drawn, as the age data show that both apatite generations were formed with a difference of about 50 Ma. In this sense, the Si incorporation rather refers to a general phenomenon that magmatic apatites potentially have in common and their otherwise different composition rather confirms their independent formation (at different times).

The hydrothermal apatite, on the other hand, generally shows low Si values (<0.01 apfu). These apatites, which appear as remobilised masses, occur paragenetically with quartz (i.e. an environment saturated in Si), but show consistently very low Si contents, as well as very low REE contents. Therefore, it can be assumed that the Si incorporation at very low temperatures is not favored by the apatite and quartz entirely consumes the available Si. Due to the formation of discrete REE minerals (mostly monazite in contact with apatite, Fig. 3E, G), the REEs are also completely consumed by REE minerals and incorporation into apatite is inhibited.

Another important indicator for hydrothermal apatite formation is the Sr content. Chakhmouradian et al. (2017) and the recent review of carbonatitic apatites by Guo et al. (2024) generally agree that Sr depletion is typical for hydrothermal apatites, while Sr enrichment indicates the magmatic origin of most apatites. However, the hydrothermal apatites of Nooitgedacht show no Sr depletion (compared to the magmatic generations). In fact, the present study shows a systematic increase of Sr in hydrothermal apatites. This tendency in turn fits in with the exceptions of Sr (±REE, Na)-rich replacement zones and overgrowths during the hydrothermal phase of some dolomite(−bearing) carbonatites described by Chakhmouradian et al. (2017). Even if the characterisation as dolomite(−bearing) carbonatite applies to the quartz-Fe-dolomite-calcite carbonatite, the “common” calcite carbonatite, which shows the same Sr-enrichment trend in apatite, is excluded (as no noteworthy dolomite content is present). It must therefore be assumed that the phenomenon of the exception in Sr enrichment in hydrothermal apatites is not limited to dolomite-bearing carbonatites.

Sr-rich apatite at Nooitgedacht is typically associated with Fe-dolomite, which leads to the assumption that the Fe-dolomite was formed as a secondary phase from a dissolution-reprecipitation reaction caused by the interaction of a Fe-Mg-rich fluid and carbonate phases. While the calcite-carbonatite typically contains Sr-rich calcite (as the first calcite generation), the quartz-dolomite-carbonatite exhibits rather low Sr-calcite, but a higher proportion of discrete strontium minerals (e.g. strontianite and theoretically more precursor burbankite). Both situations offer sufficient potential for Sr remobilisation during the post-magmatic hydrothermal stage. Sr incorporation into dolomite is much lower than into calcite by the common factor of 2:1 (calcite:dolomite) at hydrothermal/low temperature conditions (150–350 °C; Jacobson and Usdowski, 1976, and references therein). A corresponding redistribution of Sr during the formation of Fe-dolomite (with limited incorporation of Sr) may have favored the incorporation of Sr into apatite during co-precipitation.

Another feature that particularly affects the hydrothermal apatites from both the calcite carbonatites (apatite type II) and the quartz-rich lenses (apatite type V) of the quartz-Fe-dolomite-calcite carbonatites is the potential incorporation of CO_3^{2-} as part of the hydrothermal overprinting. Santos and Clayton (1995) demonstrated that in particular apatite formed by metasomatic/(hydrothermal) fluids may contain relatively high concentrations of carbonate. However, the incorporation of CO_3^{2-} in apatite does not only depend on total C content in the fluid, but also on the C speciation in the fluid (Santos and Clayton, 1995). Apatite formed by a fluid with carbonate ions in solution offers a higher vulnerability to incorporate CO_3^{2-} into apatite than fluids that contain molecular CO_2. The calcite dissolution during hydrothermal

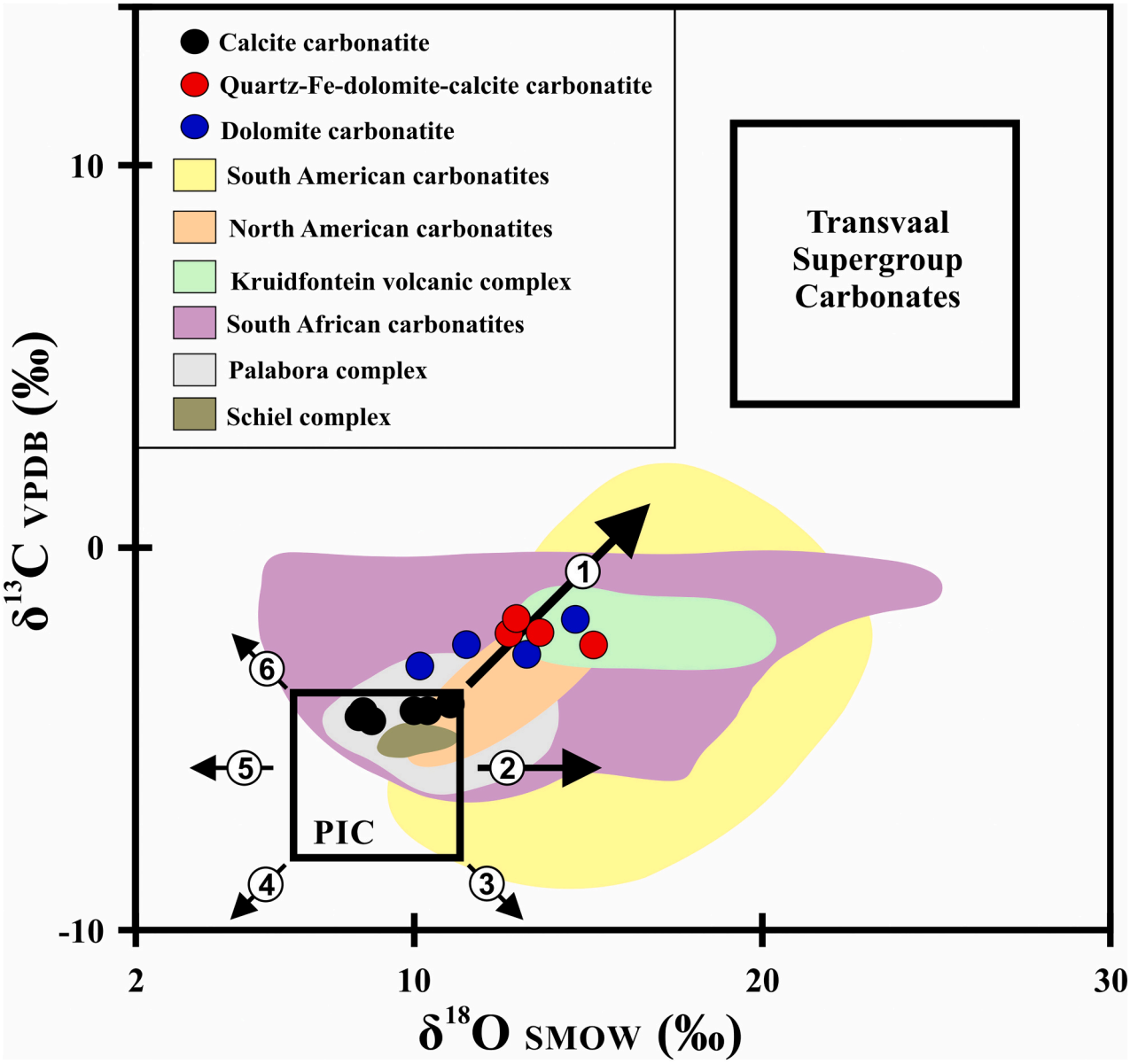

Fig. 11. Stable carbon-oxygen isotope composition of the Nooitgedacht Carbonatite Complex. South and North American carbonatites (Bell, 2005), the Kruidfontein Volcanic Complex (Schürmann et al., 1997), South African carbonatites (Horstmann and Verwoerd, 1997), the Palabora complex (Munro and Harris, 2023), the Schiel complex (Horstmann and Verwoerd, 1997) and Transvaal Supergroup Carbonates (Frauenstein et al., 2009) are plotted for comparison. PIC = Primary Igneous Carbonatites (Taylor et al., 1967). Arrows indicate: (1) Crustal contamination / high temperature fractionation, (2) low temperature alteration, (3) degassing, (4) metamorphism, (5) high temperature alteration, (6) sea water influence. While calcite carbonatite shows an isotope composition that falls into the PIC box, quartz-Fe-dolomite-calcite carbonatite and dolomite carbonatite isotopic compositions tends to increase following the direction of crustal contamination and/or high temperature fractionation.

overprinting (as described above) is predestined to ensure a corresponding carbonate enrichment in the fluid. The strong overlap of hydrothermal apatite types II and V shows that these apatites must have been formed under very similar conditions. It is particularly noticeable that apatite types II and V are chemically almost identical. However, they cannot have been formed by the same event, as both apatites were formed around 50 Ma apart.

5.3. Appearance and nature of REE mineralization

Petrographic and mineral chemical results indicate that the Nooitgedacht Complex underwent three distinct crystallization phases, namely the ortho-magmatic, carbothermal late-magmatic, and hydrothermal post-magmatic stages (Fig. 5; plus, a subordinate supergene stage). While calcite carbonatites (carbonatite type I) are mostly characterized by minerals of the ortho-magmatic stage, quartz-Fe-dolomite-calcite carbonatites (carbonatite type II) show a major impact of late-magmatic and post-magmatic (hydrothermal) mineralization. Although both carbonatites show the same ortho-magmatic mineral assemblages, follow the same crystallization sequence, and only differ in the intensity of the different mineralization stages (this allows them to be included in a combined paragenetic framework, Fig. 5), they are still to be regarded as separate intrusions. Based on geochronological data, and mineral chemical and textural differences (e.g., see primary apatite composition and appearance), it is evident that both carbonatites reflect separate melt batches. Even so, the coincident mineralization, particularly with respect to REE mineralization, is used to decipher general processes that are not specific to the individual carbonatite intrusions.

It is well known that magmatic REE mineralization in carbonatites follows typical enrichment processes. These magmatic mineralisations can generally be characterized by an early consumption of REE or a late enrichment of REE (in residual brine-melts/carbothermal fluids), resulting in the formation of corresponding REE-bearing minerals or discrete REE mineral phases. In particular, apatite (as an important REE-bearing mineral phase) is a common candidate for incorporating significant quantities of REE (due to its high occurrence in carbonatites). Early fractionation of apatite can extract a substantial quantity of REE from a carbonatite melt, while inhibition of such REE consumption can result in REE enrichment in residual melts/fluids. As shown above REE enrichment in apatite is the highest (in relative terms) in the primary magmatic pill-shaped apatite (apatite type I; <0.08 apfu, <1.4 wt%). However, both, whole rock data and mineralogical observations confirm that REE enrichment is generally highest in quartz-Fe-dolomite-calcite carbonatite, where REE mineralization formed mainly during the hydrothermal post-magmatic stage (mainly as monazite with minor REE carbonates) and apparently subordinately during the late-magmatic carbothermal stage (mainly as potential burbankite, and minor monazite and bastnäsite).

The formation of monazite is always closely linked to the occurrence of apatite (Fig. 5). While the appearance of monazite as rims around magmatic apatite (minor presence; Fig. 4E) indicates the precipitation of monazite at the expense of apatite during the late-magmatic carbothermal stage (e.g. Giebel et al., 2019a,b; Kempe and Götze, 2002; Walter et al., 1995), the formation as disseminated grains or clusters in the quartz – apatite – Fe-dolomite association suggest a common mobilization and subsequent coupled precipitation of REE^{3+}, PO_4^{3-}, F^-, Fe^{2+}, Mg^{2+} and SiO_2 during the post-magmatic hydrothermal stage. The provision of Ca^{2+} and CO_3^{2-} is probably ensured by the in-situ dissolution of calcite.

In respect to the relatively lower abundance of magmatic phosphates (apatite) in comparison to the hydrothermal formation of phosphates (apatite and monazite), it becomes obvious that a local dissolution and reprecipitation neither of REE nor of P from primary apatite is sufficient to provide the needed amount of these elements to form the corresponding hydrothermal phosphate (±REE) mineral association. Apatite and monazite that form in the hydrothermal stage significantly exceeds the potential provision of REE and P from magmatic apatite (on a in situ/local scale). This suggests that the enrichment of these elements must have been done elsewhere. As the majority of the country rocks consist of quartzite and dolomitic limestone and are not enriched in phosphates, mobilization of P and REE from these lithologies can be ruled out. In addition, the quartz-Fe-dolomite-calcite carbonatite, which appear in the centre of the complex and is enclosed by the calcite carbonatite (poorly overprinted), which in turn represents the contact to the country rock, shows the strongest hydrothermal overprinting and thus, in addition to the highest REE enrichment, also the highest secondary phosphate enrichment. This suggests that the hydrothermal fluid potentially originated from deeper parts of the intrusion and probably followed the same or similar path of ascent as the quartz-Fe-dolomite calcite carbonatite without strong interaction with the enveloping calcite carbonatite and adjacent country rock (at the erosion level). Although an exact source of the REE and P cannot be proven, it can be assumed that in deeper levels a significantly stronger and large-scale dissolution of apatite could have caused a corresponding enrichment. Considering that a carbonatite with no significant formation of hydrothermal apatite has P_2O_5 contents typically below 1 wt%, and the hydrothermally phosphate-enriched carbonatites (including the typical proportion of quartz-apatite lenses in quartz-Fe-dolomite-calcite carbonatites) have an average content of >5 wt% P_2O_5, it can be concluded that an enrichment of P_2O_5 by a factor of ~5 (or higher) is required to ensure the corresponding enrichment in the hydrothermal stage (given that the source shows a similar phosphate budget as hydrothermally unaffected carbonatite at the erosion level).

Furthermore, it can be assumed that a large-scale dissolution of discrete magmatic REE minerals (mainly burbankite) could support a corresponding REE mobilization and redistribution. Burbankite is a common mineral in carbonatites that typically forms in late-magmatic stages from a 'brine-melt', enriched in alkalis and REE (Prokopyev et al., 2016; Anenburg et al., 2020). However, as burbankite (or in cases carbocernaite) is an extremely unstable alkali-REE carbonate (Anenburg et al., 2020; Nikolenko et al., 2022) it is often (easily) dissolved during later stages (e.g., by hydrothermal overprint). It can often only be identified by the presence of typical replacement assemblages (e.g., strontianite, baryte, REE carbonates) inside hexagonal pseudomorphs (Zaitsev et al., 1998; Andersen et al., 2017; Kozlov et al., 2020; Giebel et al., 2017). Preservation of burbankite or carbocernaite is uncommon. Considering the very common presence of mineral assemblages of baryte, strontianite and bastnäsite in hexagonal replacement textures (Fig. 4G), which are typically associated with destabilisation and decomposition of alkali REE carbonates (Anenburg et al., 2020; Kozlov et al., 2020; Anenburg et al., 2021), it can be assumed that remobilisation and redistribution of REE from precursor burbankite (or carbocernaite) is very likely.

Even if the REEs could be efficiently redistributed and locally enriched during post-magmatic overprinting, findings from other deposits and experimental data indicate that the original REE budget is actually controlled by the mineralization of the late-magmatic carbothermal ('brine melt') stage. Despite this fact, REE mineralization in carbonatites is frequently attributed to hydrothermal processes (e.g., Ngwenya, 1994, Trofanenko et al., 2016, Broom-Fendley et al., 2016; Broom-Fendley et al., 2017a,b, Marien et al., 2018; Dietzel et al., 2019). However, as magmatic REE mineralization (with unstable alkali-REE-carbonates probably being the most frequent mineralization), is typically dissolved and REE are remobilized, the importance of magmatic REE enrichment is often underestimated. Thus, REE mineral formation from hydrothermal fluids can easily be (wrongly) interpreted as the original REE mineralization, although it only represents an efficient REE redistribution.

5.4. Crustal contamination and its consequences in the Nooitgedacht Complex

Recent studies have shown that crustal contamination (potentially appearing during magma ascent and emplacement) may play an important role in carbonatite magmatism. This can result in a significant change in the isotopic and geochemical composition of the carbonatite melt (Anenburg et al., 2020; Giebel et al., 2019a,b; Wei et al., 2023; Zheng et al., 2023). In particular, the stability and abundance of specific silicate minerals in the carbonatite magma can increase significantly due to the external introduction of Si (and Al). While the external introduction of elements is limited to the specific solubility of certain elements in the melt, a repeated melt – wall-rock/xenolith interaction/resorption can favor an efficient interplay of 'element oversaturation – mineral precipitation – repeated element introduction'. However, even if, by this means, silicate phases (some are also aluminum-rich), can be formed to a larger amount despite the low Si (and very low Al) solubility, only mineral phases that require a relatively low silica activity ($aSiO_2$) can be formed. Mineral phases that only show stability at high $aSiO_2$ cannot be easily formed in carbonatite magmas, which characteristically have a low $aSiO_2$ (Barker, 2001). The low $aSiO_2$ (at magmatic conditions) prevents, for example, the formation of quartz. A sufficient increase of $aSiO_2$ (in a carbonatitic system) can only be achieved under low temperature conditions (in combination with an adequate Si introduction), which is typically feasible at hydrothermal (rather than magmatic) stages. Therefore, it is essential to differentiate the impacts of contamination throughout a complex's magmatic and post-magmatic phases.

The presence of silicate xenoliths within the quartz-Fe-dolomite-calcite carbonatite of Nooitgedacht clearly indicates an introduction of crustal material during the ascent of carbonatitic magma. A

corresponding interaction between the carbonate melt and the xenolith, with a corresponding enrichment of Si in the melt, could be potentially expected. Mineralogically, however, no significant magmatic interactions between the carbonatitic melt and the xenoliths can be observed. The enhanced formation of silicates and formation of distinct magma-xenolith interaction zones (e.g., mica or pyroxene seams) is absent. On the other hand, the elemental introduction by wall rock/xenolith interactions does not only support the formation of certain silicates, but may also cause compositional variations in non-silicate minerals. Apatite that experiences a britholite substitution (see above) due to contamination-related Si introduction, for example, may cause a distinct consumption of REEs from the carbonatite melt at an early magmatic stage (Anenburg, 2020; Broom-Fendley et al., 2017a,b; Giebel et al., 2019a,b; Lu et al., 2021; Prowatke and Klemme, 2006; Zhang et al., 2022). Consequently (given the necessity that sufficient quantities of apatite were formed), the REE cannot undergo further enrichment in the melt (Giebel et al., 2019a,b; Krestianinov et al., 2021), leading to a notable reduction in the formation of distinct REE minerals in higher evolved magmas (e.g., Lofdal and Okorusu, Namibia; Songwe Hill, Malawi; Amba Dongar, India; Bodeving et al., 2017; Broom-Fendley et al., 2017a,b; Cangelosi et al., 2020; Doroshkevich et al., 2009). The carbonatites of Nooitgedacht (both calcite and quartz-Fe-dolomite-calcite carbonatites), however, show a predominant apatite composition that do not clearly indicate a noticeable influence of magmatic contamination. While at magmatic temperatures apatite favours an REE enrichment due to britholite substitution, at lower (hydrothermal or supergene) temperatures the REE enrichment in apatite is typically controlled by the belovite substitution (Doroshkevich et al., 2009). A predominant influence of the belovite substitution in apatites at Nooitgedacht therefore indicates a low temperature (certainly post-magmatic) overprint. Post-magmatic hydrothermal or supergene processes can furthermore enable the precipitation of silicate minerals, such as quartz (see above). This may explain the prevalent occurrence of quartz in quartz-Fe-dolomite-calcite carbonatites. The presence of Si in a hydrothermal (or meteoric) fluid, in turn, may affect the mobility of REE and formation of REE mineralization in carbonatites. In fact, in particular the quartz-Fe-dolomite-calcite carbonatite, exhibits a significant post-magmatic occurrence of REE-carbonates that are typically intergrown with quartz. Furthermore, this mineral assemblage is paragenetically accompanied by baryte, celestite and strontianite, which conclusively suggests that a mobilization, transportation and deposition of REE, Si, S, and Ba (and Sr) occurred simultaneously during late-stage hydrothermal processes in the carbonatites of Nooitgedacht. While sulfur may serve as an efficient transport ligand to mobilize REE (in particular in quartz-saturated fluids) even at low temperature conditions (Cui et al., 2020), phosphate represents a strong binding ligand that causes the direct precipitation of REE phosphates (Johannesson et al., 1995; Han, 2020). Consequently, monazite can often be found in direct contact with apatite in the strongly overprinted quartz-apatite lenses.

Si enrichment might generally be caused (1) by the introduction of Si-rich external fluids, (2) by Si enrichment in circulating fluids in contact with the silicate host rock, or (3) by fluids resorbing silicate xenoliths embedded in the carbonatite. While the first two scenarios would presumably lead to increased quartz formation, especially in contact zones between carbonatite and host rock (resulting in the fluid being buffered relatively rapidly), the last scenario would ensure that the fluid is repeatedly enriched in Si through interaction with the silicate xenoliths (distributed throughout the entire carbonatite), thus favoring a more regular distribution of quartz in the carbonatite. It is therefore considered that the magmatic introduction of silicate xenoliths in particular has achieved a strong post-magmatic impact at Nooitgedacht. The lack of magmatic interaction between the carbonatite magma and silicate xenoliths, in contrast, suggests that the carbonatite magma already reached a relatively low temperature during its intrusion, which inhibited a pronounced interaction. At higher temperatures, intensive interactions would be expected (e.g., Kaiserstuhl, Giebel et al., 2019b).

5.5. C-O isotope composition

The C-O isotope data of the Nooitgedacht Complex follows a trend from primary igneous carbonatites towards higher C and O isotope values. Within this trend, the carbonatites can be subdivided into two groups that reflect (1) the calcite carbonatite (primary igneous carbonatite isotopic composition) and (2) quartz-Fe-dolomite-calcite and dolomite carbonatites (deviant trend with a higher C and O isotopic composition). A similar trend has been observed by Horstmann and Verwoerd (1997) and Schürmann et al. (1997) for other South African carbonatites. While a deviation of C and O isotope values from the primary igneous carbonatite field may be caused by various low and high temperature processes (mostly post-magmatic alteration; Santos and Clayton, 1995), in particular a deviation to higher $\delta^{13}C$ and $\delta^{18}O$ resulted from Rayleigh fractionation or crustal contamination (isotope exchange with country rocks; Deines, 1970). Calcite carbonatites from Schiel and Palabora (as prominent representatives of South African carbonatites; Eriksson and Reczko, 1995) show relatively primitive compositions, which indicates low Rayleigh fractionation. Both carbonatites, largely retain their primary igneous C and O isotopy and plot within or in close proximity to the primary igneous carbonatite box (Taylor et al., 1967). In contrast, the Kruidfontein carbonatites (as the closest neighbouring carbonatite and part of the South African occurrences (plotted in Fig. 11) does not retain their primary C and O isotopic values ($\delta^{13}C = -1$ to -13 and $\delta^{18}O = 11$ to 18). Schürmann et al. (1997) explained this deviation by late-magmatic/metasomatic process. Santos and Clayton (1995) interpreted a similar trend from South American carbonatites as a result of magmatic modification and secondary alteration by host rock assimilation and hydrothermal processes, respectively. While the “common” calcite carbonatites (Type 1) obviously lack any evidence of xenolith entrainment and intense wall-rock interaction (hence reflecting a less influenced carbonatite melt), for quartz-Fe-dolomite calcite carbonatite and dolomite carbonatite, contamination by wall-rock interaction cannot be excluded and seems to be reasonable.

A hypothetic interpretation that the dolomitic limestones (host rock) may have caused isotopic contamination that could explain the observed deviation at Nooitgedacht would further expect that a much stronger influence would primarily affect the directly contacting calcite carbonatite. However, while calcite carbonatite shows unaffected values, the apparently affected quartz-Fe-dolomite-calcite and dolomite carbonatites are mostly situated in the centre of the complex, enveloped by calcite carbonatite. At a first glance, this argues against contamination as the origin of the isotope deviation, and fractionated crystallization becomes a more likely process to explain the isotopic variation. The carbonatite age dating, however, reveals the *presence* of two separate intrusions, which does not allow a discussion of a direct evolutionary relationship between the carbonatites. On the other hand, dolomite-enriched and dolomite carbonatites are generally regarded as higher evolved carbonatites (Yaxley et al., 2021). The possibility of a more pronounced Rayleigh fractionation of the potentially relatively higher evolved (later emplaced) carbonatite intrusions, which formed independently of the appearance of the calcite carbonatite, can therefore not be ruled out in principle. A temporally divergent intrusion, furthermore, allows simpler conclusions about a potential introduction of xenoliths into the quartz-Fe-dolomite-calcite-carbonatite, as the later intruding carbonatite magma may have been exposed to other intrusion conditions and could have used different paths for its ascent. It must be noted, however, that the identified xenoliths are exclusively siliceous in nature (which would exclusively cause elevated oxygen isotope values); no carbonate xenoliths were found in the investigated samples. Due to the small volume of the late carbonatites, a sufficient contamination with wall-rock material (at the direct host-rock interface) during ascent (without significant carbonate xenolith introduction) could be suggested to produce the observed isotopic modification. In conclusion, it is not possible to specify which particular process is responsible for the isotopic variations of the Nooitgedacht carbonatites or whether it could

even be a combination of both processes. Even if both carbonatites form in the same complex, they are individual intrusions and it can be assumed that they derive from different magma flows, which possibly utilized the same system of trans-crustal zones of weakness for their ascent and originated from a similar source, but probably did not share exactly the same ascent conduit.

5.6. Evolution of Nooitgedacht Carbonatite Complex

The evolution of the Nooitgedacht complex can be grouped into 6 stages:

Stage-I: The initial stage is marked by the formation of syenite, which is indicated by field observations and the entrainment of Ta-U rich pyrochlores (formed in syenitic magma; pyrochlore type I) into later intruding calcite carbonatite (first-generation of carbonatites) (Fig. 12A, B). Syenites are found in close association with the carbonatites. The presence of these pyrochlores suggests that the syenitic melt was enriched in high-field-strength elements (HFSEs) such as tantalum and uranium.

Stage-II: Induces the early magmatic emplacement of calcite carbonatite, either as a single plug or as successive intrusions (Fig. 12B). Syenitic pyrochlores that got entrained into the carbonatitic melt has been eroded and overgrown by a carbonatitic pyrochlore generation (pyrochlore type II).

Stage-III: Approximately 50 million years after the first carbonatite intrusion, a second generation of carbonatite was emplaced at Nooitgedacht. This phase is characterized by a calcite carbonatite comprising a slightly higher dolomite proportion. This stage likely coincides with renewed tectonic activity, which reactivated the magmatic system and facilitated the emplacement of the evolved carbonatitic magma. The intrusion of a second generation of calcite carbonatite near the centre of the main calcite carbonatite intrusion forms a small ring complex (Fig. 12C). Late-magmatic carbothermal overprint ('brine melting' stage) caused the formation of discrete REE minerals (monazite and bastnäsite).

Stage-IV: Following the magmatic emplacement, post-magmatic hydrothermal alteration significantly modified the carbonatites. This stage is characterized by the interaction of carbonatites with hydrothermal fluids, leading to recrystallization, element mobilization, and the precipitation of secondary sulfates, phosphates, and silicates (Fig. 12D). Alteration processes likely enriched or redistributed rare earth elements (REEs), HFSEs, and other critical metals. Magmatic pyrochlores were overprinted and enriched in REE (pyrochlore type III). Hydrothermal activity could have been driven by residual magmatic fluids or external fluid infiltration, creating complex mineralogical and chemical assemblages.

Stage V: The final stage of magmatic activity recorded the emplacement of dolomite carbonatite as dikes along structural weaknesses, suggesting a more advanced degree of differentiation and Mg-enrichment (Fig. 12E). The dike-like morphology implies intrusion during a late tectonic phase, potentially associated with localized extension or stress regimes. The dolomite composition, as opposed to calcite, indicates increased fractionation, marking the final magmatic stage of carbonatite evolution. It is important to mention at this point

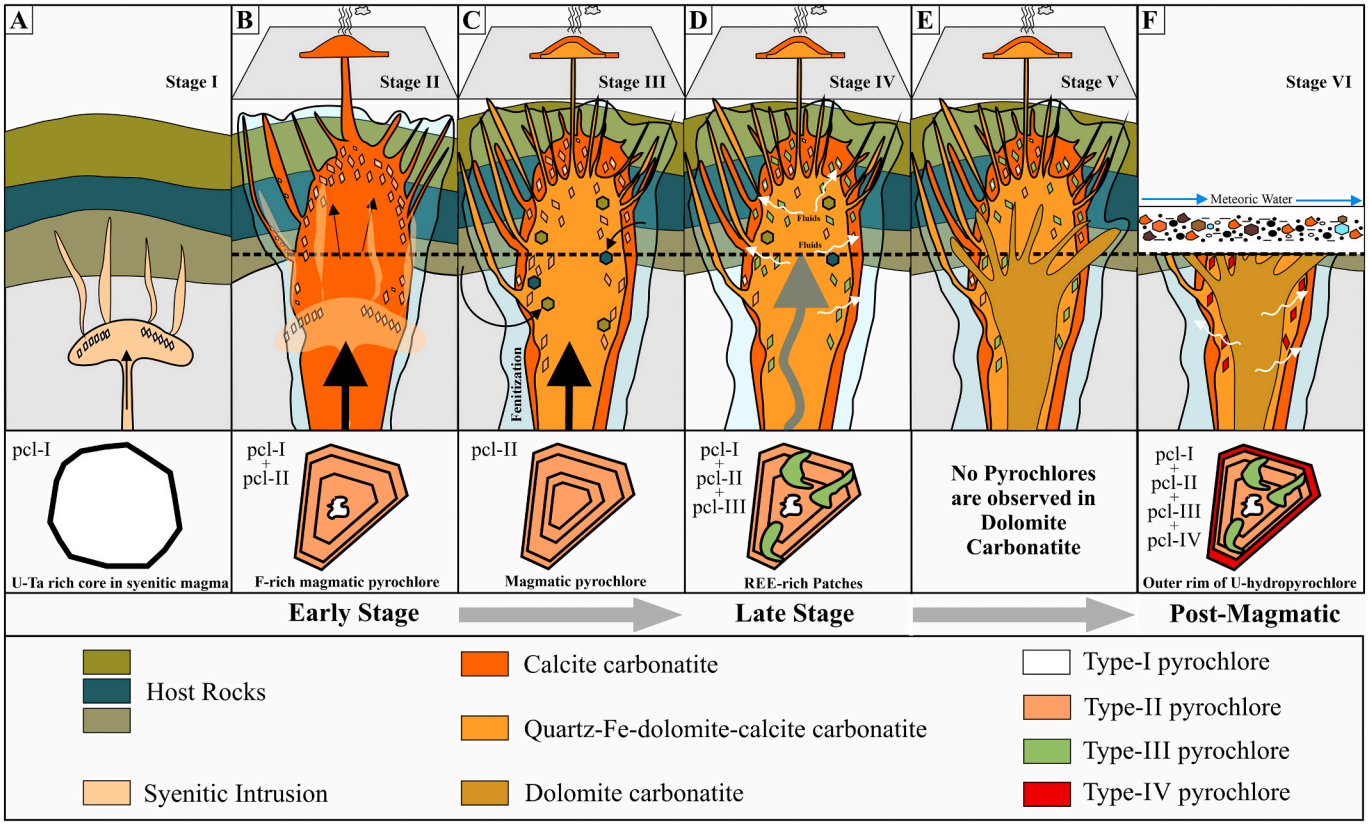

Fig. 12. Evolution of the Nooitgedacht carbonatite vs. evolution of pyrochlore. (A) Formation of early U-Ta rich pyrochlore (type I) in a silicate melt (potentially syenite). (B) Intrusion of calcite carbonatite (~1330 Ma). Pyrochlore of probably syenitic origin (pyrochlore type I) was entrained and resorbed during the ascent of the calcite carbonatite. Magmatic/oscillatory pyrochlore (type II) overgrows resorbed cores of type I pyrochlore. Fenitization of country rocks took place. (C) A second generation of slightly dolomite enriched calcite carbonatite (preserved as quartz-Fe-dolomite-calcite carbonatite) intruded the early calcite carbonatite at ~1280 Ma. (D) Stage-IV reflects the hydrothermal overprint of the calcite carbonatites (generation 1 and 2). This resulted in the formation of quartz-Fe-dolomite-calcite carbonatite (previously present as second generation of calcite carbonatite). Hydrothermal fluids overprinted magmatic pyrochlores in the form of REE-rich patches (pyrochlore type III). (E) Emplacement of dolomite carbonatite. (F) Weathering and supergene alteration took place in stage-VI, narrow U-hydropyrochlore (pyrochlore type IV) formed around the previously formed pyrochlores.

that the temporal position (and corresponding evolutionary stage) of the dolomite carbonatite, in relation to the other carbonatites, is uncertain due to the lack of age data. Based on its geometry (dykes), crosscutting relationships and observations in previous studies, the dolomite carbonatite has been assigned to the very last intrusion stage.

Stage VI: The final stage in the evolution of the carbonatites involves supergene processes, where near-surface weathering and oxidation affected the exposed carbonatite bodies (Fig. 12F). This stage is marked by the formation of secondary minerals such as iron oxides, hydroxides, and caused a further overprint of pyrochlore (pyrochlore type IV).

The multi-stage evolution of the Nooitgedacht carbonatites, from primary magmatic processes through hydrothermal alteration to supergene enrichment, illustrates a dynamic and prolonged geological history. The significant age gap between magmatic stages suggests episodic tectonic reactivation, while the hydrothermal and supergene stages emphasize the role of post-magmatic processes in shaping the mineralogical and geochemical characteristics of the carbonatites. This comprehensive evolution underscores the importance of integrating magmatic, hydrothermal, and surface processes when evaluating the genesis and economic potential of carbonatite systems. Further studies focusing on fluid inclusion studies, and geochemical modeling are essential to deepen our understanding of the mantle sources, magmatic evolution, and post-magmatic modifications of these unique systems.

6. Conclusion

This research contributes valuable insights into the evolution and petrogenesis of the Nooitgedacht Carbonatite Complex, highlighting their mineralogical and geochemical diversity. The primitive mantle-normalized trace elements and chondrodite normalized REE patterns combined with mineralogical observations suggest an HFSE enrichment in early stage calcite carbonatite and LREE enrichment due to redistribution by hydrothermal overprint in later stage quartz-Fe-dolomite-calcite carbonatite, respectively.

Although, the hydrothermal overprint produced a significant REE mineralization, as described from numerous other carbonatite occurrences, the mineralogical evidence point to a magmatic enrichment of REE and a post-magmatic highly efficient redistribution and local accumulation of REE (and phosphorus) caused by re-mobilization of the previously formed (magmatic) REE budget of the complex. The close (hydrothermal) association of REE minerals (±phosphates and baryte) with quartz suggests a common transportation of REE, P, S, Ba and Si in the same fluid. While most of these elements were probably re-mobilized from carbonatitic material, Si was mobilized by the alteration/resorption of entrained silicate xenoliths (Nebo granite). An efficient hydrothermal redistribution of REE in combination with Si (and probably S; e.g., Cui et al., 2020) seems to be a common phenomenon that appears in numerous carbonatites and can result in significant accumulations of REE (e.g., Twyfelskupje and Kieshöhe complexes, Namibia). In order to decipher the role of Si for the efficient re-mobilization of REE under hydrothermal conditions, further research in this direction is required.

This study, furthermore, highlights apatite and pyrochlore as key minerals in the Nooitgedacht carbonatites to identify distinct evolutionary stages. Their geochemical signatures demonstrate the critical role of magmatic to postmagmatic (hydrothermal/supergene) processes in the formation of economic deposits. In particular, pyrochlore demonstrated a high potential as a proxy for carbonatite evolution. Clearly defined compositional variations proof a distinct evolutionary stage (magmatic, hydrothermal or supergene) of pyrochlore formation.

The new U-Pb age data for calcite carbonatite (~1330 Ma) and quartz-Fe-dolomite-calcite carbonatite (~1280 Ma) shows an age gap of approximately 50 million years between the carbonatite intrusions, indicating a prolonged magmatic activity and the episodic reuse of trans-crustal pathway systems. However, to understand the importance of the reuse of ascending pathways studies on further (similar) carbonatite complexes are needed.

CRediT authorship contribution statement

Mohsin Raza: Writing – original draft, Visualization, Software, Resources, Methodology, Investigation, Funding acquisition, Formal analysis, Data curation, Conceptualization. **R. Johannes Giebel:** Writing – review & editing, Visualization, Validation, Supervision, Software, Resources, Project administration. **Sebastian Staude:** Writing – review & editing, Validation, Software, Methodology, Formal analysis. **Aratz Beranoaguirre:** Writing – review & editing, Visualization, Software, Methodology, Investigation, Formal analysis, Data curation. **Jochen Kolb:** Writing – review & editing, Validation, Supervision, Resources, Project administration, Funding acquisition, Conceptualization. **Gregor Markl:** Writing – review & editing, Visualization, Validation, Data curation, Conceptualization. **Benjamin F. Walter:** Writing – review & editing, Visualization, Validation, Supervision, Resources, Project administration, Funding acquisition, Conceptualization.

Declaration of competing interest

The authors declare that they have no known competing financial interests or personal relationships that could have appeared to influence the work reported in this paper.

Acknowledgments

The financial assistance provided to Mohsin Raza by the Higher Education Commission of Pakistan (HEC Pakistan) Ref. 1(2)/HRD/OSS-III/2021/HEC/19542 and the German Academic Exchange Service (DAAD) Ref. 91818586, Graduate School for Climate and Environment (GRACE) and Karlsruhe House of Young Scientists (KHYS) for the doctoral studies is acknowledged with gratitude. This study was supported by DFG grants WA 3116/4-1 and INST 121384/213-1. The authors express their gratitude to Elisabeth Eiche, Beate Ötzel, Claudia Mössner, Denker Maya, and Kristian Nikoloski from the LERA facilities at KIT for their valuable assistance in the analysis and material preparation. The authors would like to thank Gary O'Connor for introducing them to the Nooitgedacht complex and emphasizing on specific outcrops. We would also like to thanks Dr. Tobias Kluge for his valuable discussions on isotopes that improved the manuscript. The handling editor, Dr. Tomas Magna and Dr. Vincenza Guarino are thanked for handling the manuscript and Dr. Shuo Xue and anonymous reviewers are also thanked for their very thorough and constructive reviews that significantly improved the quality of the manuscript.

Appendix A. Supplementary data

Supplementary data to this article can be found online at https://doi.org/10.1016/j.chemer.2025.126249.

References

Andersen, A.K., Clark, J.G., Larson, P.B., Donovan, J.J., 2017. REE fractionation, mineral speciation, and supergene enrichment of the Bear Lodge carbonatites, Wyoming, USA. Ore Geol. Rev. 89, 780–807. https://doi.org/10.1016/j.oregeorev.2017.06.025.

Anenburg, M., 2020. Rare earth mineral diversity controlled by REE pattern shapes. Mineral. Mag. 84, 629–639. https://doi.org/10.1180/MGM.2020.70.

Anenburg, M., Mavrogenes, J.A., 2018. Carbonatitic versus hydrothermal origin for fluorapatite REE-Th deposits: experimental study of REE transport and crustal "antiskarn" metasomatism. Am. J. Sci. 318, 335–366. https://doi.org/10.2475/03.2018.03.

Anenburg, M., Mavrogenes, J.A., Bennett, V.C., 2020. The fluorapatite P–REE–Th vein deposit at Nolans Bore: genesis by carbonatite metasomatism. J. Petrol. 61, 3. https://doi.org/10.1093/PETROLOGY/EGAA003.

Anenburg, M., Broom-Fendley, S., Chen, W., 2021. Formation of rare earth deposits in carbonatites. Elements 17, 327–332. https://doi.org/10.2138/GSELEMENTS.17.5.327.

Anenburg, M., Panikorovskii, T.L., Jennings, E.S., Shendrik, R.Y., Antonov, A.A., Gavrilenko, V., 2024. An Apatite-Group Praseodymium Carbonate Fluoroxybritholite: hydrothermal synthesis, crystal structure, and implications for

natural and synthetic Britholites. Inorg. Chem. 63. https://doi.org/10.1021/acs.inorgchem.4c01490, 11788–1180.
Armstrong, J.T., 1991. Quantitative Elemental Analysis of Individual Microparticles with Electron Beam Instruments. In: Electron Probe Quantitation. Springer US, Boston, MA, pp. 261–315. https://doi.org/10.1007/978-1-4899-2617-3_15.
Atencio, D., Andrade, M.B., Christy, A.G., Gieré, R., Kartashov, P.M., 2010. The pyrochlore supergroup of minerals: nomenclature. Can. Mineral. 48, 673–698. https://doi.org/10.3749/canmin.48.3.673.
Bambi, A.C.J.M., Costanzo, A., Gonçalves, A.O., Melgarejo, J.C., 2012. Tracing the chemical evolution of primary pyrochlore from plutonic to volcanic carbonatites: the role of fluorine. Mineral. Mag. 76, 377–392. https://doi.org/10.1180/MINMAG.2012.076.2.07.
Barker, D.S., 2001. Calculated silica activities in carbonatite liquids. Contrib. Mineral. Petrol. 141, 704–709. https://doi.org/10.1007/S004100100281/METRICS.
Bell, K., 2005. Igneous rocks: carbonatites. Encycl. Geol. 217–233. https://doi.org/10.1016/B0-12-369396-9/00296-3.
Bell, K., Simonetti, A., 2010. Source of parental melts to carbonatites-critical isotopic constraints. Mineral. Petrol. 98, 77–89. https://doi.org/10.1007/S00710-009-0059-0.
Bence, A.E., Albee, A.L., 1968. Empirical correction factors for the electron microanalysis of silicates and oxides. J. Geol. 382–403. https://doi.org/10.1086/627339.
Benkó, Z., Molnár, K., Magna, T., Rapprich, V., Palcsu, L., Pour, O., Čejková, B., Futó, I., Czuppon, G., 2021. Combined petrography, noble gas, stable isotope and fluid inclusion chemistry of carbonatites from Uganda: implications for the origin of the carbonatite melt in continental rift setting. Chem. Geol. 578. https://doi.org/10.1016/J.CHEMGEO.2021.120213.
Beranoaguirre, A., Vasiliev, I., Gerdes, A., 2022. In situ LA-ICPMS U-Pb dating of sulfates: applicability of carbonate reference materials as matrix-matched standards. Geochronology 4, 601–616. https://doi.org/10.5194/GCHRON-4-601-2022.
Bodeving, S., Williams-Jones, A.E., Swinden, S., 2017. Carbonate–silicate melt immiscibility, REE mineralising fluids, and the evolution of the Lofdal Intrusive Suite, Namibia. Lithos 268, 383–398. https://doi.org/10.1016/j.lithos.2016.11.024.
Broom-Fendley, S., Styles, M.T., Appleton, J.D., Gunn, G., Wall, F., 2016. Evidence for dissolution-reprecipitation of apatite and preferential LREE mobility in carbonatite-derived late-stage hydrothermal processes. Amer. Mineral. 101 (3), 596–611. https://doi.org/10.2138/am-2016-5502CCBY.
Broom-Fendley, S., Brady, A.E., Horstwood, M.S.A., Woolley, A.R., Mtegha, J., Wall, F., Dawes, W., Gunn, G., 2017a. Geology, geochemistry and geochronology of the Songwe Hill carbonatite, Malawi. J. Afr. Earth Sci. 134, 10–23. https://doi.org/10.1016/J.JAFREARSCI.2017.05.020.
Broom-Fendley, S., Brady, A.E., Wall, F., Gunn, G., Dawes, W., 2017b. REE minerals at the Songwe Hill carbonatite, Malawi: HREE-enrichment in late-stage apatite. Ore Geol. Rev. 81, 23–41. https://doi.org/10.1016/J.OREGEOREV.2016.10.019.
Cangelosi, D., Broom-Fendley, S., Banks, D., Morgan, D., Yardley, B., 2020. Light rare earth element redistribution during hydrothermal alteration at the Okorusu carbonatite complex, Namibia. Mineral. Mag. 84 (1), 49–64. https://doi.org/10.1180/mgm.2019.54.
Chakhmouradian, A.R., 2006. High-field-strength elements in carbonatitic rocks: geochemistry, crystal chemistry and significance for constraining the sources of carbonatites. Chem. Geol. 235, 138–160. https://doi.org/10.1016/J.CHEMGEO.2006.06.008.
Chakhmouradian, A.R., Mitchell, R.H., 1998. Lueshite, pyrochlore and monazite-(Ce) from apatite-dolomite carbonatite, Lesnaya Varaka complex, Kola Peninsula, Russia. Mineral. Mag. 62, 769–782. https://doi.org/10.1180/002646198548151.
Chakhmouradian, A.R., Wall, F., 2012. Rare earth elements: minerals, mines, magnets (and more). Elements 8, 333–340. https://doi.org/10.2113/GSELEMENTS.8.5.333.
Chakhmouradian, A.R., Reguir, E.P., Zaitsev, A.N., Couëslan, C., Xu, C., Kynický, J., Mumin, A.H., Yang, P., 2017. Apatite in carbonatitic rocks: compositional variation, zoning, element partitioning and petrogenetic significance. Lithos 274–275, 188–213. https://doi.org/10.1016/J.LITHOS.2016.12.037.
Cui, H., Zhong, R., Xie, Y., Yuan, X., Liu, W., Brugger, J., Yu, C., 2020. Forming sulfate- and REE-rich fluids in the presence of quartz. Geology 48 (2), 145–148. https://doi.org/10.1130/G46893.1.
de Oliveira Cordeiro, P.F., Brod, J.A., Palmieri, M., de Oliveira, C.G., Barbosa, E.S.R., Santos, R.V., Gaspar, J.C., Assis, L.C., 2011. The Catalão I niobium deposit, central Brazil: resources, geology and pyrochlore chemistry. Ore Geol. Rev. 41 (1), 112–121. https://doi.org/10.1016/j.oregeorev.2011.06.013.
Deines, P., 1970. The carbon and oxygen isotopic composition of carbonates from the Oka carbonatite complex, Quebec, Canada. Geochim. Cosmochim. Acta 34, 1199–1225. https://doi.org/10.1016/0016-7037(70)90058-X.
Demény, A., Ahijado, A., Casillas, R., Vennemann, T.W., 1998. Crustal contamination and fluid/rock interaction in the carbonatites of Fuerteventura (Canary Islands, Spain): a C, O, H isotope study. Lithos 44, 101–115. https://doi.org/10.1016/S0024-4937(98)00050-4.
Dietzel, C.A., Kristandt, T., Dahlgren, S., Giebel, R.J., Marks, M.A., Wenzel, T., Markl, G., 2019. Hydrothermal processes in the Fen alkaline-carbonatite complex, southern Norway. Ore Geol. Rev. 111, 102969. https://doi.org/10.1016/j.oregeorev.2019.102969.
Doroshkevich, A.G., Viladkar, S.G., Ripp, G.S., Burtseva, M.V., 2009. Hydrothermal REE mineralization in the Amba Dongar carbonatite complex, Gujarat, India. Can. Mineral. 47 (5), 1105–1116. https://doi.org/10.3749/canmin.47.5.1105.
Dumańska-Słowik, M., Pieczka, A., Tempesta, G., Olejniczak, Z., Heflik, W., 2014. "Silicified" pyrochlore from nepheline syenite (mariupolite) of the Mariupol Massif, SE Ukraine: a new insight into the role of silicon in the pyrochlore structure. Am. Mineral. 99, 2008–2017. https://doi.org/10.2138/AM-2014-4896.
Elburg, M.A., Cawthorn, R.G., 2017. Source and evolution of the alkaline Pilanesberg Complex, South Africa. Chem. Geol. 455, 148–165. https://doi.org/10.1016/j.chemgeo.2016.10.007.
Eriksson, P.G., Reczko, B.F.F., 1995. The sedimentary and tectonic setting of the Transvaal Supergroup floor rocks to the Bushveld complex. J. Afr. Earth Sci. 21, 487–504. https://doi.org/10.1016/0899-5362(95)00111-5.
Ferguson, J., 1973. The Pilanesberg Alkaline Igneous Province. Trans. Geol. Soc. S. Afr. 76 (3), 249–270.
Frauenstein, F., Veizer, J., Beukes, N., Van Niekerk, H.S., Coetzee, L.L., 2009. Transvaal Supergroup carbonates: implications for Paleoproterozoic δ18O and δ13C records. Precambrian Res. 175 (1–4), 149–160. https://doi.org/10.1016/j.precamres.2009.09.005.
Friedman, I., O'Neil, J.R., 1977. Compilation of Stable Isotope Fractionation Factors of Geochemical Interest (No. 440-KK). https://doi.org/10.3133/pp440KK.
Friese, A.E., Reimold, W.U., Layer, P.W., 2003. 40Ar-39Ar dating of and structural information on tectonite-bearing faults in the Witwatersrand Basin: evidence for multi-stage, tectono-thermal activity in the central Kaapvaal Craton. S. Afr. J. Geol. 106 (1), 41–70. https://doi.org/10.2113/1060041.
Gerdes, A., Zeh, A., 2006. Combined U-Pb and Hf isotope LA-(MC-)ICP-MS analyses of detrital zircons: comparison with SHRIMP and new constraints for the provenance and age of an Armorican metasediment in Central Germany. Earth Planet. Sci. Lett. 249, 47–61. https://doi.org/10.1016/J.EPSL.2006.06.039.
Gerdes, A., Zeh, A., 2009. Zircon formation versus zircon alteration — new insights from combined U–Pb and Lu–Hf in-situ LA-ICP-MS analyses, and consequences for the interpretation of Archean zircon from the Central Zone of the Limpopo Belt. Chem. Geol. 261, 230–243. https://doi.org/10.1016/J.CHEMGEO.2008.03.005.
Johannes Giebel, R. Johannes, Gauert, C.D., Marks, M.A., Costin, G., Markl, G., 2017. Multi-stage formation of REE minerals in the Palabora Carbonatite Complex, South Africa. Amer. Mineral. 102 (6), 1218–1233. https://doi.org/10.2138/am-2017-6004.
Giebel, R. Johannes, Marks, M.A.W., Gauert, C.D.K., Markl, G., 2019a. A model for the formation of carbonatite-phoscorite assemblages based on the compositional variations of mica and apatite from the Palabora Carbonatite Complex, South Africa. Lithos 324–325, 89–104. https://doi.org/10.1016/J.LITHOS.2018.10.030.
Giebel, R.J., Parsapoor, A., Walter, B.F., Braunger, S., Marks, M.A.W., Wenzel, T., Markl, G., 2019b. Evidence for magma–wall rock interaction in carbonatites from the Kaiserstuhl Volcanic Complex (Southwest Germany). J. Petrol. 60, 1163–1194. https://doi.org/10.1093/PETROLOGY/EGZ028.
Gittins, J., Harmer, R.E., 1997. What is ferrocarbonatite? A revised classification. J. Afr. Earth Sci. 25, 159–168. https://doi.org/10.1016/S0899-5362(97)00068-7.
Gold, D.P., 1986. Carbonatites, Diatremes, and Ultra-alkaline Rocks in the Oka Area, Quebec: May 22–23, 1986. Geol. Assoc, Canada.
Gonçalves, G.O., Lana, C., Scholz, R., Buick, I.S., Gerdes, A., Kamo, S.L., Corfu, F., Marinho, M.M., Chaves, A.O., Valeriano, C., Nalini, H.A., 2016. An assessment of monazite from the Itambé pegmatite district for use as U–Pb isotope reference material for microanalysis and implications for the origin of the "Moacyr" monazite. Chem. Geol. 424, 30–50. https://doi.org/10.1016/J.CHEMGEO.2015.12.019.
Goodenough, K.M., Schilling, J., Jonsson, E., Kalvig, P., Charles, N., Tuduri, J., Deady, E. A., Sadeghi, M., Schiellerup, H., Müller, A., Bertrand, G., Arvanitidis, N., Eliopoulos, D.G., Shaw, R.A., Thrane, K., Keulen, N., 2016. Europe's rare earth element resource potential: an overview of REE metallogenetic provinces and their geodynamic setting. Ore Geol. Rev. 72, 838–856. https://doi.org/10.1016/j.oregeorev.2015.09.019.
Guarino, V., Wu, FY., Melluso, L., et al., 2017. U–Pb ages, geochemistry, C–O–Nd–Sr–Hf isotopes and petrogenesis of the Catalão II carbonatitic complex (Alto Paranaíba Igneous Province, Brazil): implications for regional-scale heterogeneities in the Brazilian carbonatite associations. Int. J. Earth Sci. (Geol. Rundsch) 106, 1963–1989. https://doi.org/10.1007/s00531-016-1402-4.
Gudelius, D., Marks, M.W., Markl, G., Nielsen, T.F.D., Kolb, J., Walter, B.F., 2023. The origin of ultramafic complexes with melilitolites and carbonatites: a petrological comparison of the Gardiner (E Greenland) and Kovdor (Russia) intrusions. J. Petrol. 64, 1–26. https://doi.org/10.1093/PETROLOGY/EGAD036.
Guo, H., Tuduri, J., Nabyl, Z., Erdmann, S., Li, X., Gaillard, F., 2024. Rare earth elements in apatite: a proxy for unravelling carbonatite melt compositions. Earth Planet. Sci. Lett. 642, 118863. https://doi.org/10.1016/j.epsl.2024.118863.
Han, K.N., 2020. Characteristics of precipitation of rare earth elements with various precipitants. Minerals 10 (2), 178. https://doi.org/10.3390/min10020178.
Harmer, R.E., 1999. The Petrogenetic Association of Carbonatite and Alkaline Magmatism: constraints from the Spitskop Complex, South Africa. J. Petrol. 40, 525–548. https://doi.org/10.1093/PETROJ/40.4.525.
Hatton, C.J., Schweitzer, J.K., 1995. Evidence for synchronous extrusive and intrusive Bushveld magmatism. J. Afr. Earth Sci. 21, 579–594. https://doi.org/10.1016/0899-5362(95)00103-4.
Hogarth, D.D., 1977. Classification and nomenclature of the pyrochlore group. Am. Mineral. 62 (5–6), 403–410.
Hogarth, D.D., Williams, C.T., Jones, P., 2000. Primary zoning in pyrochlore group minerals from carbonatites. Mineral. Mag. 64, 683–697. https://doi.org/10.1180/002646100549544.
Horstmann, U.E., Verwoerd, W.J., 1997. Carbon and oxygen isotope variations in southern African carbonatites. J. Afr. Earth Sci. 25, 115–136. https://doi.org/10.1016/S0899-5362(97)00065-1.
Horstwood, M.S.A., Košler, J., Gehrels, G., Jackson, S.E., McLean, N.M., Paton, C., Pearson, N.J., Sircombe, K., Sylvester, P., Vermeesch, P., Bowring, J.F., Condon, D.J., Schoene, B., 2016. Community-derived standards for LA-ICP-MS U-(Th-)Pb geochronology–uncertainty propagation, age interpretation and data reporting.

Geostand. Geoanal. Res. 40, 311–332. https://doi.org/10.1111/J.1751-908X.2016.00379.X/ABSTRACT.

Hou, Z., Liu, Y., Tian, S., Yang, Z., Xie, Y., 2015. Formation of carbonatite-related giant rare-earth-element deposits by the recycling of marine sediments. Sci. Rep. 5 (1), 10231. https://doi.org/10.1038/srep10231 (2015).

Humphreys-Williams, E.R., Zahirovic, S., 2021. Carbonatites and global tectonics. Elements 17, 339–344. https://doi.org/10.2138/GSELEMENTS.17.5.339.

Jacobson, R.L., Usdowski, H.E., 1976. Partitioning of strontium between calcite, dolomite and liquids: an experimental study under higher temperature diagenetic conditions, and a model for the prediction of mineral pairs for geothermometry. Contrib. Mineral. Petrol. 59, 171–185. https://doi.org/10.1007/BF00371306.

Jago, B.C., Gittins, J., 1993. Pyrochlore crystallization in carbonatites: the role of fluorine. S. Afr. J. Geol. 96, 149–159.

Jochum, K.P., Weis, U., Stoll, B., Kuzmin, D., Yang, Q., Raczek, I., Jacob, D.E., Stracke, A., Birbaum, K., Frick, D.A., Günther, D., Enzweiler, J., 2011. Determination of reference values for NIST SRM 610-617 glasses following ISO guidelines. Geostand. Geoanal. Res. 35, 397–429. https://doi.org/10.1111/J.1751-908X.2011.00120.X.

Johannesson, K.H., Lyons, W.B., Stetzenbach, K.J., Byrne, R.H., 1995. The solubility control of rare earth elements in natural terrestrial waters and the significance of PO_4^{3-} and CO_3^{2-} in limiting dissolved rare earth concentrations: a review of recent information. Aquat. Geochem. 1, 157–173. https://doi.org/10.1007/BF00702889.

Jones, A.P., Genge, M., Carmody, L., 2013. Carbonate melts and carbonatites. Rev. Mineral. Geochem. 75, 289–322. https://doi.org/10.2138/rmg.2013.75.10.

Kamenetsky, V.S., Doroshkevich, A.G., Elliott, H.A.L., Zaitsev, A.N., 2021. Carbonatites: contrasting, complex, and controversial. Elements 17, 307–314. https://doi.org/10.2138/GSELEMENTS.17.5.307.

Kempe, U., Götze, J., 2002. Cathodoluminescence (CL) behaviour and crystal chemistry of apatite from rare-metal deposits. Mineral. Mag. 66, 151–172. https://doi.org/10.1180/0026461026610019.

Ketcham, R.A., 2015. Technical note: calculation of stoichiometry from EMP data for apatite and other phases with mixing on monovalent anion sites. Am. Mineral. 100, 1620–1623. https://doi.org/10.2138/AM-2015-5171/MACHINEREADABLECITATION/RIS.

Khan, A., Faisal, S., Ullah, Z., Ali, L., Ghaffari, A., Nawab, J., Rashid, M.U., 2021. Pyrochlore-group minerals from the Loe-Shilman Carbonatite Complex, NW Pakistan: implications for evolution of carbonatite system. Period. Mineral. 90 (2), 277–287. https://doi.org/10.13133/2239-1002/17360.

Khromova, E.A., Doroshkevich, A.G., Sharygin, V.V., Izbrodin, L.A., 2017. Compositional evolution of Pyrochlore-group minerals in carbonatites of the Belaya Zima Pluton, Eastern Sayan. Geol. Ore Depos. 59, 752–764. https://doi.org/10.1134/S1075701517080037/METRICS.

Kozlov, E., Fomina, E., Sidorov, M., Shilovskikh, V., Bocharov, V., Chernyavsky, A., Huber, M., 2020. The Petyayan-Vara carbonatite-hosted rare earth deposit (Vuoriyarvi, NW Russia): mineralogy and geochemistry. Minerals 10 (1), 73. https://doi.org/10.3390/min10010073.

Krestianinov, E., Amelin, Y., Neymark, L.A., Aleinikoff, J.N., 2021. U-Pb systematics of uranium-rich apatite from Adirondacks: inferences about regional geological and geochemical evolution, and evaluation of apatite reference materials for in situ dating. Chem. Geol. 581, 120417. https://doi.org/10.1016/J.CHEMGEO.2021.120417.

Lana, C., Gonçalves, G.O., Mazoz, A., Buick, I., Kamo, S., Scholz, R., Wang, H., Moreira, H., Babinski, M., Queiroga, G., 2022. Assessing the U-Pb, Sm-Nd and Sr-Sr isotopic compositions of the Sumé apatite as a reference material for LA-ICP-MS analysis. Geostand. Geoanal. Res. 46, 71–95. https://doi.org/10.1111/GGR.12413/ABSTRACT.

Le Maitre, R.W., 2002. Igneous Rocks: A Classification and Glossary of Terms Cambridge. Cambridge Univ. Press, UK.

Lee, M.J., Lee, J.I., Garcia, D., Moutte, J., Williams, C.T., Wall, F., Kim, Y., 2006. Pyrochlore chemistry from the Sokli phoscorite-carbonatite complex, Finland: implications for the genesis of phoscorite and carbonatite association. Geochem. J. 40, 1–13. https://doi.org/10.2343/GEOCHEMJ.40.1.

Lee, W.J., Wyllie, P.J., 1997. Liquid immiscibility between nephelinite and carbonatite from 1.0 to 2.5 GPa compared with mantle melt compositions. Contrib. Mineral. Petrol. 127, 1–16. https://doi.org/10.1007/S004100050261/METRICS.

Lottermoser, B.G., England, B.M., 1988. Compositional variation in pyrochlores from the Mt Weld carbonatite laterite, Western Australia. Mineral. Petrol. 38, 37–51. https://doi.org/10.1007/BF01162480/METRICS.

Lu, J., Chen, W., Ying, Y., Jiang, S., Zhao, K., 2021. Apatite texture and trace element chemistry of carbonatite-related REE deposits in China: implications for petrogenesis. Lithos 398–399, 106276. https://doi.org/10.1016/J.LITHOS.2021.106276.

Ludwig, K.R., 2003. User's Manual for Isoplot 3.00: A Geochronological Toolkit for Microsoft Excel, Berkeley. Geochronological Center, Berkeley, p. 70.

Lumpkin, G.R., Ewing, A.C., 1996. Geochemical alteration of pyrochlore group minerals: Betafite subgroup. Am. Mineral. 81, 1237–1248. https://doi.org/10.2138/am-1996-9-1022.

Marien, C., Dijkstra, A.H., Wilkins, C., 2018. The hydrothermal alteration of carbonatite in the Fen Complex, Norway: mineralogy, geochemistry, and implications for rare-earth element resource formation. Mineral. Mag. 82 (S1), S115–S131. https://doi.org/10.1180/minmag.2017.081.070.

McDonough, W.F., Sun, S.S., 1995. The composition of the Earth. Chem. Geol. 120 (3–4), 223–253. https://doi.org/10.1016/0009-2541(94)00140-4.

McDowell, F.W., McIntosh, W.C., Farley, K.A., 2005. A precise 40Ar–39Ar reference age for the Durango apatite (U–Th)/He and fission-track dating standard. Chem. Geol. 214, 249–263. https://doi.org/10.1016/J.CHEMGEO.2004.10.002.

Migdisov, A., A.E., W.-J., 2014. Hydrothermal transport and deposition of the rare earth elements by fluorine-bearing aqueous liquids. Mineral. Deposita 49, 987–997. https://doi.org/10.1007/s00126-014-0554-z.

Millonig, L.J., Gerdes, A., Groat, L.A., 2012. U–Th–Pb geochronology of meta-carbonatites and meta-alkaline rocks in the southern Canadian Cordillera: a geodynamic perspective. Lithos 152, 202–217. https://doi.org/10.1016/J.LITHOS.2012.06.016.

Mitchell, R.H., 2005. Carbonatites and carbonatites and carbonatites. Can. Mineral. 43, 2049–2068. https://doi.org/10.2113/GSCANMIN.43.6.2049.

Mitchell, R.H., Liferovich, R.P., 2005. A structural study of the perovskite series Na0.75Ln0.25Ti0.5Nb0.5O3. J. Solid State Chem. 178, 2586–2593. https://doi.org/10.1016/J.JSSC.2005.05.016.

Munro, J., Harris, C., 2023. A high-δ18O mantle source for the 2.06 Ga Phalaborwa Igneous Complex, South Africa? J. Petrol. 64 (9), egad063. https://doi.org/10.1093/petrology/egad063.

Nasraoui, M., Bilal, E., 2000. Pyrochlores from the Lueshe carbonatite complex (Democratic Republic of Congo): a geochemical record of different alteration stages. J. Asian Earth Sci. 18, 237–251. https://doi.org/10.1016/S1367-9120(99)00056-5.

Ngwenya, B.T., 1994. Hydrothermal rare earth mineralisation in carbonatites of the Tundulu complex, Malawi: processes at the fluid/rock interface. Geochim. Cosmochim. Acta 58 (9), 2061–2072. https://doi.org/10.1016/0016-7037(94)90285-2.

Nikolenko, A.M., Stepanov, K.M., Roddatis, V., Veksler, I.V., 2022. Crystallization of bastnäsite and burbankite from carbonatite melt in the system La (CO_3) F-$CaCO_3$-Na2CO3 at 100 MPa. Am. Mineral. 107 (12), 2242–2250. https://doi.org/10.2138/am-2022-8064.

Prokopyev, I.R., Borisenko, A.S., Borovikov, A.A., Pavlova, G.G., 2016. Origin of REE-rich ferrocarbonatites in southern Siberia (Russia): implications based on melt and fluid inclusions. Mineral. Petrol. 110, 845–859.

Prowatke, S., Klemme, S., 2006. Trace element partitioning between apatite and silicate melts. Geochim. Cosmochim. Acta 70, 4513–4527. https://doi.org/10.1016/J.GCA.2006.06.162.

Santos, R.V., Clayton, R.N., 1995. Variations of oxygen and carbon isotopes in carbonatites: a study of Brazilian alkaline complexes. Geochim. Cosmochim. Acta 59, 1339–1352. https://doi.org/10.1016/0016-7037(95)00048-5.

Schmidt, M.W., Giuliani, A., Poli, S., 2024. The origin of carbonatites—combining the rock record with available experimental constraints. J. Petrol. 65 (10), egae105. https://doi.org/10.1093/petrology/egae105.

Schürmann, L.W., Horstmann, U.E., Cloete, H.C.C., 1997. Geochemical and stable isotope patterns in altered volcaniclastic and intrusive rocks of the Kruidfontein carbonatite complex, South Africa. J. Afr. Earth Sci. 25, 77–101. https://doi.org/10.1016/S0899-5362(97)00063-8.

Scoates, J.S., Friedman, R.M., 2008. Precise age of the platiniferous merensky reef, Bushveld complex, South Africa, by the U-Pb zircon chemical abrasion ID-TIMS technique. Econ. Geol. 103, 465–471. https://doi.org/10.2113/GSECONGEO.103.3.465.

Sharma, S.K., Sharma, T., 1969. Oxygen isotope fractionation factor between CO_2 and CO_3^{2-}. Int. J. Mass Spectrom. 2 (4–5), 367–371. https://doi.org/10.1016/0020-7381(69)80031-8.

Stoppa, F., 2021. Evolution and involution of carbonatite thoughts. Elements 17, 303–304. https://doi.org/10.2138/GSELEMENTS.17.5.303.

Stoppa, F., Schiazza, M., Rosatelli, G., Castorina, F., Sharygin, V.V., Ambrosio, F.A., Vicentini, N., 2019. Italian carbonatite system: from mantle to ore-deposit. Ore Geol. Rev. 114, 103041. https://doi.org/10.1016/J.OREGEOREV.2019.103041.

Taylor, H.P., Frechen, J., Degens, E.T., 1967. Oxygen and carbon isotope studies of carbonatites from the Laacher See District, West Germany and the Alnö District, Sweden. Geochim. Cosmochim. Acta 31, 407–430. https://doi.org/10.1016/0016-7037(67)90051-8.

Teiber, H., Marks, M.A.W., Arzamastsev, A.A., Wenzel, T., Markl, G., 2015. Compositional variation in apatite from various host rocks: clues with regards to source composition and crystallization conditions. Neu. Jb. Mineral. 192, 151–167. https://doi.org/10.1127/NJMA/2015/0277.

Trofanenko, J., Williams-Jones, A.E., Simandl, G.J., Migdisov, A.A., 2016. The nature and origin of the REE mineralization in the Wicheeda Carbonatite, British Columbia, Canada. Econ. Geol. 111, 199–223. https://doi.org/10.2113/econgeo.111.1.199.

Vasyukova, O.V., Williams-Jones, A.E., 2023. A new model for the origin of pyrochlore: evidence from the St Honoré Carbonatite, Canada. Chem. Geol. 632, 121549. https://doi.org/10.1016/j.chemgeo.2023.121549.

Verplanck, P.L., Mariano Jr., A.N., A.M., 2016. Rare earth element ore geology of carbonatites. In: Rare Earth and Critical Elements in Ore Deposits. Soc. Econ. Geol., Inc., pp. 5–32

Verwoerd, W.J., 1967. The carbonatites of South Africa and South Africa, a nuclear raw materials investigation primarily for the Atomic Energy Board, Department of mines. Geol. Sur. S. Afr. 452. https://www.abebooks.co.uk/Carbonatites-South-Africa-Nuclear-Raw-Materials/31738475905/bd.

Verwoerd, W.J., 1993. Update on carbonatites of South Africa and Namibia. S. Afr. J. Geol. 96, 75–95.

Verwoerd, W.J., 2006. The Pilanesberg Alkaline Province. In: Johnson, M.R., Anhaeusser, C.R., Thomas, R.J. (Eds.), The Geology of South Africa. Geol. Soc. S. Afr, Johannesburg, pp. 380–393.

Viladkar, S.G., Sorokhtina, N.V., 2021. Evolution of pyrochlore in carbonatites of the Amba Dongar complex, India. Mineral. Mag. 85, 554–567. https://doi.org/10.1180/MGM.2021.50.

Wall, F., Williams, C.T., Woolley, A.R., Nasraoui, M., 1996. Pyrochlore from weathered carbonatite at Lueshe, Zaire. Mineral. Mag. 60, 731–750. https://doi.org/10.1180/MINMAG.1996.060.402.03.

Walraven, F., Frick, C., Lubala, R.T., 1992. Pb-isotope geochronology of the Schiel complex, Northern Transvaal, South Africa. J. Afr. Earth Sci. (and the Middle East) 15, 103–110. https://doi.org/10.1016/0899-5362(92)90011-Z.

Walter, A.V., Nahon, D., Flicoteaux, R., Girard, J.P., Melfi, A., 1995. Behaviour of major and trace elements and fractionation of REE under tropical weathering of a typical apatite-rich carbonatite from Brazil. Earth Planet. Sci. Lett. 136, 591–602. https://doi.org/10.1016/0012-821X(95)00195-I.

Walter, B.F., Parsapoor, A., Braunger, S., Marks, M.A.W., Wenzel, T., Martin, M., Markl, G., 2018. Pyrochlore as a monitor for magmatic and hydrothermal processes in carbonatites from the Kaiserstuhl volcanic complex (SW Germany). Chem. Geol. 498, 1–16. https://doi.org/10.1016/J.CHEMGEO.2018.08.008.

Walter, B.F., Giebel, R.J., Steele-MacInnis, M., Marks, M.A.W., Kolb, J., Markl, G., 2021. Fluids associated with carbonatitic magmatism: a critical review and implications for carbonatite magma ascent. Earth Sci. Rev. 215, 103509. https://doi.org/10.1016/J.EARSCIREV.2021.103509.

Wan, Y., Wang, X., Chou, I.M., Li, X., 2021. Role of sulfate in the transport and enrichment of REE in hydrothermal systems. Earth Planet. Sci. Lett. 569, 117068. https://doi.org/10.1016/J.EPSL.2021.117068.

Wei, C. wan, Xu, C., Song, W. lei, Chen, W., Shi, A., Li, Z., Fan, C., 2023. Heavy rare earth element and crustal-derived silicon enrichment in Huayangchuan carbonatites, Qinling orogenic belt. Lithos 436–437, 106987. https://doi.org/10.1016/J.LITHOS.2022.106987.

Williams, C.T., Wall, F., Woolley, A.R., Phillipo, S., 1997. Compositional variation in pyrochlore from the Bingo carbonatite, Zaïre. J. Afr. Earth Sci. 25, 137–145. https://doi.org/10.1016/S0899-5362(97)00066-3.

Williams-Jones, E.A., Artas, M.A., 2014. Rare earth element transport and deposition by hydrothermal fluids. Acta Geol. Sin. Engl. Ed. 88, 472–474. https://doi.org/10.1111/1755-6724.12373_28.

Woolley, A.R., Kjarsgaard, B.A., 2008. Carbonatite Occurrences of the World: Map and Database. https://doi.org/10.4095/225115.

Yaxley, G.M., Kjarsgaard, B.A., Jaques, A.L., 2021. Evolution of carbonatite magmas in the upper mantle and crust. Elements 17, 315–320. https://doi.org/10.2138/GSELEMENTS.17.5.315.

Yaxley, G.M., Anenburg, M., Tappe, S., Decree, S., Guzmics, T., 2022. Carbonatites: classification, sources, evolution, and emplacement. Annu. Rev. Earth Planet. Sci. 50, 261–293. https://doi.org/10.1146/ANNUREV-EARTH-032320-104243/1.

Yudovskaya, M., Masunte, T., Kinnaird, J.A., Mwenze, T., Ueckermann, H., Iaccheri, L., Borisovsky, S., Bolhar, R., 2023. An extension of the Rooiberg Group and Upper Zone of the Bushveld Complex in the northernmost Waterberg segment. Precambrian Res. 399, 107228. https://doi.org/10.1016/J.PRECAMRES.2023.107228.

Zaitsev, A.N., Wall, F., Le Bas, M.J., 1998. REE-Sr-Ba minerals from the Khibina carbonatites, Kola Peninsula, Russia: their mineralogy, paragenesis and evolution. Mineral. Mag. 62 (2), 225–250. https://doi.org/10.1180/002646198547594.

Zaitsev, A.N., Williams, C.T., Wall, F., Zolotarev, A.A., 2012. Evolution of chemical composition of pyrochlore group minerals from phoscorites and carbonatites of the Khibina alkaline massif. Geol. Ore Depos. 54, 503–515. https://doi.org/10.1134/S1075701512070094/METRICS.

Zaitsev, A.N., Spratt, J., Shtukenberg, A.G., Zolotarev, A.A., Britvin, S.N., Petrov, S.V., Kuptsova, A.V., Antonov, A.V., 2021. Oscillatory- and sector-zoned pyrochlore from carbonatites of the Kerimasi volcano, Gregory rift, Tanzania. Mineral. Mag. 85, 532–553. https://doi.org/10.1180/MGM.2020.101.

Zhang, W., Terry Chen, W., Zhang, X.C., Tang, Y.W., 2022. The trace element chemistry of quartz in carbonatite-related REE deposits: implication for REE exploration. Ore Geol. Rev. 149, 105068. https://doi.org/10.1016/J.OREGEOREV.2022.105068.

Zheng, X., Liu, Y., Smith, M.P., Kynický, J., Hou, Z., 2023. Carbonatitic magma fractionation and contamination generate rare earth element enrichment and mineralization in the Maoniuping Giant REE Deposit, SW China. J. Petrol. 64, 1–36. https://doi.org/10.1093/PETROLOGY/EGAD037.

Zurevinski, S.E., Mitchell, R.H., 2004. Extreme compositional variation of Pyrochlore-group minerals at the Oka Carbonatite Complex, Quebec: evidence of magma mixing? Can. Mineral. 42, 1159–1168. https://doi.org/10.2113/GSCANMIN.42.4.1159.